

PARSEC-SCALE BLAZAR MONITORING: FLUX AND POLARIZATION VARIABILITY

DANIEL C. HOMAN¹, ROOPESH OJHA², JOHN F. C. WARDLE³, AND DAVID H. ROBERTS³,
 Physics Department MS057, Brandeis University

Waltham, MA 02454

MARGO F. ALLER⁴, HUGH D. ALLER⁴, AND PHILIP A. HUGHES⁴
 Radio Astronomy Observatory, University of Michigan
 Ann Arbor, MI 48109

Submitted to the Astrophysical Journal

ABSTRACT

We present analysis of the flux and polarization variability of parsec scale radio jets from a dual-frequency, six-epoch, VLBA polarization experiment monitoring 12 blazars. The observations were made at 15 and 22 GHz at bimonthly intervals over 1996. Here we analyze the flux, fractional polarization, and polarization position angle behavior of core regions and jet features, considering both the linear trends of these quantities with time and more rapid fluctuations about the linear trends. The dual frequency nature of the observations allows us to examine spectral evolution, to separate Faraday effects from changes in magnetic field order, and also to deduce empirical estimates for the uncertainties in measuring properties of VLBI jet features (see the Appendix). Our main results include the following:

On timescales $\gtrsim 1$ year, we find that jet features generally decayed in flux, with older features decaying more slowly than younger features. Using the decay rates of jet features from six sources, we find $I \propto R^{-1.3 \pm 0.1}$. Short term fluctuations in flux tended to be fractionally larger in core regions than in jet features, with the more compact core regions having the larger fluctuations. We find significant spectral index changes in the core regions of four sources. Taken together these are consistent with an outburst-ejection cycle for new jet components. Jet features from one source showed a significant spectral flattening over time.

Jet features either increased in fractional polarization with time or showed no significant change, with the smallest observed changes in the features at the largest projected radii. Increasing magnetic field order explains most of the increasing fractional polarization we observed. Only in the case of 3C273 is there evidence of a feature emerging from behind a Faraday depolarizing screen.

We find a number of significant polarization angle rotations including two very large ($\gtrsim 180^\circ$) rotations in the core regions of OJ287 and J1512-09. In general, polarization angle changes were of the same magnitude at both observing bands and cannot be explained by Faraday rotation. The observed polarization angle changes most likely reflect underlying changes in magnetic field structure. In jet features, four of the five observed rotations were in the direction of aligning the magnetic field with the jet axis, and coupled with the tendency of jet features to show a fractional polarization increase, this suggests increasing longitudinal field order.

Subject headings: galaxies : active — BL Lacertae objects: individual (J0738+17, OJ 287, J1310+32, J1751+09, J2005+77) — galaxies: jets — galaxies: kinematics and dynamics — quasars: individual (J0530+13, J1224+21, 3C 273, 3C 279, J1512-09, J1927+739) — galaxies: Seyfert(3C 120)

1. INTRODUCTION

We have used the National Radio Astronomy Observatory's (NRAO) Very Long Baseline Array (VLBA)⁵ to monitor the parsec scale radio jets of twelve active galactic nuclei (AGN) in both total intensity and linear polarization. The observations were taken at approximately two month intervals during 1996 at 15 and 22 GHz, and were designed to follow closely the parsec scale evolution of some of the most currently active sources being monitored by the University of Michigan Radio Astronomy Observatory (UMRAO). In Homan et al. (2001), hereafter Paper I, we published proper motion analysis from this monitoring program. Other results from the program have been presented elsewhere (e.g. Wardle et al. (1998); Homan & Wardle (1999, 2000)), and others are in preparation. In particular, the entire

data-set in the form of images, tabular data, and plots of core and jet properties versus time will be presented in Ojha et al. (in preparation, hereafter Paper III).

In this paper we analyze the flux and polarization evolution of the parsec scale radio cores and jets in our monitoring program. While many authors have made detailed studies of the kinematics of jet features (e.g. Vermeulen and Cohen (1994)), much less attention has been paid to monitoring their flux and (even more rarely) polarization behavior. Where such studies have been made, they have focused on individual objects such as 3C 273 (Unwin et al. 1985), 3C 345 (Brown, Roberts, & Wardle 1994; Lobanov & Zensus 1999), and 3C 120 (Gomez et al. 2000). This is in stark contrast to single dish monitoring programs, such as that at the UMRAO (Aller et al. 1985, 1999)

¹ Current Address: National Radio Astronomy Observatory, Charlottesville VA 22901; dhoman@nrao.edu

² Current Address: CSIRO-ATNF, Marsfield, NSW 2122, Australia; roopesh.ojha@atnf.csiro.au

³ wardle,roberts@brandeis.edu

⁴ margo,hugh,hughes@astro.lsa.umich.edu

⁵ The National Radio Astronomy Observatory is a facility of the National Science Foundation operated under cooperative agreement by Associated Universities, Inc.

which has tracked the integrated flux and polarization evolution of scores of AGN for decades at weekly or bi-weekly intervals. With the VLBA it is now possible to monitor a large number of parsec scale jets at closely spaced, regular intervals, and here we present the first analysis of data of this type for flux and polarization variability.

In this paper we focus on the overall variability properties of our sample to find common trends in the flux and polarization evolution of core regions and jet features. Section §2 describes our sample, data reduction, and model-fitting procedures. Statistical methods used in analyzing the variability properties of our VLBI observations are discussed in §3. We present and discuss our results in §4 and summarize them in §5. The Appendix explores a by-product of our variability analysis – specifically, empirical estimates of the uncertainties in the measurement of VLBI component properties.

In all calculations presented here, we assume a universe with $\Omega_M = 0.3$, $\Omega_\Lambda = 0.7$ and $H_0 = 70 \text{ km s}^{-1} \text{ Mpc}^{-1}$. For spectral index we follow the convention, $S_\nu \propto \nu^{+\alpha}$.

2. OBSERVATIONS

2.1. The Sample

We used the VLBA to conduct a series of six observations, each of 24 hour duration, at close to two month intervals during the year 1996. The observations were made at 15 GHz ($\lambda 2.0 \text{ cm}$, U-band) and 22 GHz ($\lambda 1.3 \text{ cm}$, K-band). We observed 11 target sources for six epochs and one (J1224+21) for only the last five epochs. These sources are listed in table 1. The epochs of observation during 1996 were the following: January 19th (1996.05), March 22nd (1996.23), May 27th (1996.41), July 27th (1996.57), September 27th (1996.74), and December 6th (1996.93).

The sources were chosen from those regularly monitored by the University of Michigan Radio Astronomy Observatory (UMRAO) in total intensity and polarization at 4.8, 8.0, and 14.5 GHz. They were selected according to the following criteria. (1) High total intensity: The weakest sources are about 1 Jy, the most powerful as much as 22 Jy. (2) High polarized flux: Typically over 50 mJy. (3) Violently variable: In both total and polarized intensity. Such sources are likely to be under-sampled by annual VLBI. (4) Well distributed in right ascension: This allowed us to make an optimal observing schedule.

Most of the UMRAO sources meet the first three of the above criterion. The 12 actually selected were the strongest, most violently variable sources, subject to the fourth criteria. Clearly these sources do not comprise a “complete sample” in any sense.

2.2. Data Calibration

The frequency agility and high slew speeds of the VLBA antennas were used to schedule our observations to generate maximal (u,v)-coverage. Scan lengths were kept short (13 minutes for the first two epochs and 5.5 minutes for the last four), with a switch in frequency at the end of each scan. In addition, scans of neighboring sources were heavily interleaved at the cost of some additional slew time. Each source was observed for approximately 45 minutes per frequency at each epoch.

The data were correlated on the VLBA correlator in Socorro, NM. After correlation, the data were distributed on DAT tape to Brandeis University where they were loaded into NRAO’s Astronomical Imaging Processing System (AIPS) (Bridle & Greisen 1994; Greisen 1988) and calibrated using standard

techniques for VLBI polarization observations, e.g., (Cotton 1993; Roberts, Wardle & Brown 1994). For a detailed description of our calibration steps see Paper III.

One point that bears mentioning here is our calibration of the polarization position angle (also called the Electric Vector Position Angle or EVPA). Our EVPAs were set at each epoch and at both 15 and 22 GHz by aligning the strong jet component, U1 (K1), in 3C 279 to an angle of 67° . This orientation is roughly parallel with the structural position angle for this component and is within 5° of the independently calibrated observations of Leppänen, Zensus & Diamond (1995), Taylor (1998), and Homan & Wardle (2000) whose epochs of observation bracket our own. By examining the other sources in our sample, we see no evidence that this component in 3C 279 has significant Faraday rotation at these frequencies or varies in EVPA during our observations. As a result of this EVPA calibration procedure, our internal consistency between epochs is very good with uncertainties $\approx 2 - 3$ degrees on the most robust jet features (see the Appendix).

2.3. Comparison to Single Dish Monitoring

Figure 1 compares our 15 GHz VLBA observations of J0530+13 (PKS 0528+134) and J1751+09 (OT 081) to the single dish monitoring done by the UMRAO at 14.5 GHz. The total fluxes and polarizations from our CLEAN maps agree quite well with the independent UMRAO results in all six of the VLBI epochs. The two sources plotted in figure 1 are quite compact, and the VLBA observations account for nearly all of the single dish flux. Although a detailed comparison is difficult, on the more extended sources, such as 3C 120 and 3C 273, we see a nearly constant offset between the VLBA and single dish monitoring, and the VLBI core and jet seem to account for essentially all of the observed variability in the single dish monitoring. Given this, it may be possible to use frequent single dish monitoring to help interpolate between the more widely spaced VLBI epochs to follow the evolution of parsec-scale core and jet features.

2.4. Modeling the data

To parameterize our data for quantitative analysis, we used the model fitting capabilities of the DIFMAP software package (Shepherd, Pearson & Taylor 1994, 1995) to fit the sources with a number of discrete Gaussian components. The fitting was done directly on the final, self-calibrated visibility data (i.e., in the (u,v)-plane).

Our procedures for fitting in total intensity (Stokes I) were described in Paper I. We fit the polarization in Stokes Q and U by fixing the locations (and sizes) of the I components and allowing the fluxes to vary. This procedure for fitting the polarization forces coincidence with the I components and does not account for cases where the polarization may be displaced from the total intensity. While a close inspection of the CLEAN images showed a number of cases with small displacements between total intensity and polarization peaks, our fitting procedure seemed insensitive to these and, in general, produced good agreement with the polarized fluxes and position angles observed in our CLEAN images. Our full model-fits for each source will appear in Paper III.

As discussed in §3, obtaining good estimates of the real “ 1σ ” uncertainties of VLBI model-fit parameters is a difficult problem. Our analysis procedure was designed to extract robust

variability results without a-priori knowledge of these uncertainties, and a by-product of the analysis was an empirical estimate of the accuracy with which we can measure the flux and polarization of jet features at a single epoch. These estimates are presented and discussed in the Appendix.

2.4.1. Jet Features

As we noted in Paper I, modeling a jet with Gaussian components works best with sources dominated by discrete, well separated structures. The relative flux densities, positions, and dimensions of the Gaussian components that make up a fit can be strongly correlated, particularly when jet features are closely spaced or poorly defined. In that paper, our primary concern was deciding which components were reliable tracers of the motion of jet structures. Here we are interested in the components that can be robustly analyzed for flux and polarization variability.

For this analysis we discovered that few components have sufficiently well modeled fluxes in every epoch to be treated independently. Even components that were highly accurate tracers of jet motion often had one or two epochs (at one or both frequencies) where their polarizations and/or total intensities were clearly biased by a near neighbor. With only six epochs of observation, one or two “poorly modeled” epochs would severely limit our analysis. To address this, we have simply summed together the fluxes from closely spaced components and performed our analysis on these summed fluxes. This procedure gave us a collection of core and jet *features* which consist of one or more of our Gaussian model-fit components.

The features we have chosen for analysis are listed in table 2 and illustrated below. To be considered for analysis, a feature must have existed at both frequencies for at least five epochs. For polarization analysis, we required the polarized flux to be ≥ 10 mJy and $\geq 0.5\%$ of the total intensity for at least five epochs at both frequencies. Of course, a feature must represent (to the best of our estimation) the same physical structure or pattern from epoch to epoch. In the case of core features, this means the component representing the base of the jet plus any nearby components whose fluxes cannot be reliably separated out.

In some cases, it is clear that “sub-components” of the features we analyze behave quite differently; the core regions of J0530+13 and 3C 279 are excellent examples of this. Both of these quasars have a jet component close to (and emerging from, see Paper I) the core. While these jet components seem to have distinct evolutions, we cannot confidently separate their flux and polarization behavior from that of the nearby core. We chose a robust analysis that treats each core and jet feature on equal footing. In general, the core regions we study are a combination of the ‘base-of-the-jet’ plus a nearby stationary or emerging jet feature, and in this way J0530+13 and 3C 279 are no different than the other sources in our sample.

Figures 2 through 13 display a single 15 GHz total intensity and polarization image of each source in our sample. Model components which comprise the core and jet features we follow are labeled on the images and briefly described in the figure captions. Mean properties of these features are given in table 3.

3. ANALYSIS FOR FLUX AND POLARIZATION VARIABILITY

A fundamental problem in the analysis of VLBI data for variability is knowing the real (1σ) measurement uncertainties for

⁶ In total intensity, we first divided out the mean flux at each frequency before averaging the slopes.

properties of jet features. If we knew these uncertainties robustly, it would be easy to evaluate the reality of observed flux or polarization differences between epochs.

The long VLBI reduction path includes a-priori calibration, opacity corrections, fringe fitting, band-pass solutions, self-calibration, feed leakage corrections, and model-fitting. While the uncertainties in many of these steps can be known quite well, others are much more difficult to quantify precisely, and it is difficult to combine them to obtain a robust “ 1σ ” uncertainty on the flux or polarization of a particular jet feature in a particular epoch.

3.1. Linear Trends

In the absence of robust a-priori uncertainties on the measured properties of jet features, one can still perform a linear, least-square regression assuming the data are equally weighted. With six evenly-spaced epochs, we obtained good measures (with uncertainties) for the linear changes over time in the total intensity (I), fractional polarization (m), and polarization position angle (χ) of jet features. We averaged these linear slopes between the two frequencies to obtain a single average slope over time for each jet feature⁶.

To examine any relative linear changes between the frequencies, we also computed the slopes with time in spectral index (α , $S \propto \nu^{+\alpha}$), fractional polarization ratio ($m_{ratio} = m_{15}/m_{22}$), and polarization position angle difference ($\Delta\chi = \chi_{15} - \chi_{22}$).

3.2. Fluctuations About the Linear Trends

Linear changes are interesting, but they represent the longest time scale ($\gtrsim 1$ yr) changes that our observations are sensitive to. We also wanted to examine shorter time-scale ($\lesssim 0.5$ yr) fluctuations over the six epochs. To obtain robust results for the fluctuations about the linear trends in the data, we have exploited the dual observing bands in our monitoring program. Considering the broad-band nature of synchrotron radiation, the two frequencies, 15 and 22 GHz, are closely spaced and changes at one frequency should be mirrored at the other.

To quantify this effect, we considered the deviations, Δ , in every epoch from either the best fit linear regressions over time at each frequency or the mean value at each frequency. The mean values were used only if the linear slopes at *both* frequencies were of less than 2σ significance. We formed a correlation coefficient, r from these Δ values...

$$r = \frac{\sum_j \Delta_{15j} \Delta_{22j}}{\sqrt{(\sum_i \Delta_{15i}^2)(\sum_k \Delta_{22k}^2)}}. \quad (1)$$

If the Δ values are deviations from the mean value, r is just the standard linear correlation coefficient. When $r = 1$, the fluctuations are perfectly correlated between frequencies, $r = 0$ is no correlation, and $r = -1$ is a perfect anti-correlation. A useful property of this statistic is that the correlation coefficient doesn’t require the Δ values at the two frequencies to have the same magnitude to be correlated. The fluctuations at the two frequencies must only be proportional to one another to have a strong correlation. If $\Delta_{15j} = 2 \times \Delta_{22j}$, for example, the fluctuations will be perfectly correlated. This feature compensates for some of the spectral differences that exist between the frequencies, such as a constant spectral index. A variable spectral index will, of course, degrade any correlation between the frequencies; however, polarization position angle changes generated

by variable Faraday rotation *are* detectable by this correlation coefficient because the changes at 15 GHz will always be 2.1 times those at 22 GHz.

With only five or six epochs over which we could correlate these fluctuations, it was important to assess the significances of the correlations we observed. For each jet feature, we computed r and ran a Monte Carlo simulation to compute the probability, p_r , that a correlation this strong could occur by pure chance. The Monte Carlo randomly generated Δ values pulled from a Gaussian distribution with the same variance as the data but with no intrinsic correlation between frequencies. For the cases where the original Δ values had been taken with respect to the best fit line, the randomly generated Δ values were added to this line. A new best fit line was then found and removed from the fake data to make a final set of fake Δ values to correlate. 50,000 fake data sets were generated, and p_r was the fraction of these with correlation coefficients $\geq r$ (or $\leq r$ if r was negative). For the cases where the Δ values were taken with respect to the mean at each frequency, our Monte Carlo simulation reproduced the expected theoretical probabilities (Press et al. 1995).

The correlations, r , and their significances, p_r , are given in section 4, and we consider cases with $p_r \leq 0.05$ to be statistically significant. It is interesting to examine the distribution of correlations over our whole sample, and figure 14 shows histograms of r for fluctuations in flux, fractional polarization, and polarization position angle. Plotted with the histograms are solid lines indicating the approximate distributions we would expect if the feature properties varied independently at each frequency. The histograms clearly show a very strong bias towards positive correlations indicating that real shorter term fluctuations (which appear at both frequencies) are common throughout our data set.

We also computed a measure of the amplitude of the real correlated fluctuations.

$$\Omega = r \times \frac{\sqrt{(\sum_i \Delta_{15i}^2) (\sum_k \Delta_{22k}^2)}}{(n-2)}, \quad (2)$$

where Ω is the correlated variance of the deviations from the best fit lines⁷. Here we have simply multiplied the correlation coefficient by the geometric mean of the variances at the two frequencies. The square-root of Ω gives the correlated standard deviation, a measure of the typical size of the observed fluctuations. We computed the standard deviation for the correlated fluctuations in each quantity⁸: $\delta I = \sqrt{\Omega_I}$, $\delta m = \sqrt{\Omega_m}$, and $\delta \chi = \sqrt{\Omega_\chi}$.

To place uncertainty estimates on these values, we ran a second Monte Carlo simulation similar to the one described above. In this simulation, rather than assuming no intrinsic correlation between frequency in generating the fake data, we specifically induced an intrinsic correlation of size r , matched to that in the true data. Next we found the apparent correlation between 15 and 22 GHz for all the fake data sets. From this distribution of apparent correlations, we could estimate our uncertainty in measuring a correlation of strength r . The uncertainties given in section 4 for the correlated fluctuations reflect the bounds in which 70% of the 50,000 correlations from the fake data fell about their mean.

4. RESULTS AND DISCUSSION

The analysis described in the previous section is sensitive to two types of variability:

(1) *Linear trends* which progress throughout our year long window of observations. These could be a monotonic rise or fall in flux, a continuous rotation in polarization position angle, or a steady build-up (or decay) of fractional polarization. Our analysis characterizes these changes using the best fit linear slopes with time. The timescale probed by these slopes are typically $\gtrsim 1$ year.

(2) *Fluctuations* about the linear trends which encompass variability on timescales $\lesssim 0.5$ year. These could be very short term (epoch to epoch) fluctuations, or they might represent distinct changes in the rate or sign of an otherwise continuous evolution, e.g. a jet feature that distinctly slows in its flux decay or a core region that rises then falls in flux. Our analysis quantifies the fluctuations by looking at the deviations about the best fit linear trends, correlating them between our two observing bands, and computing the standard deviation of the correlated fluctuations.

4.1. Flux Variability

Our results for linear trends in flux and fluctuations about the linear trends are summarized in table 4, and they are plotted and discussed in the following sections.

4.1.1. Linear Flux Trends

Figure 15 shows fractional flux slopes with time plotted against projected radius in the source frame. Both core and jet features are plotted, and while they have fractional slopes of similar magnitude, the distributions of the signs of the slopes are quite different. Core regions either increase or decay in flux over the year, while jet features only decay (or show no significant change) on that time-scale.

It is interesting that the fractional decay rates of the core regions do not exceed -0.5 yr^{-1} and cluster about $\sim -0.4 \text{ yr}^{-1}$, while nearly half the jet features have faster decay rates than any core region. These slopes represent the average flux trends over nearly a years time, and faster decays in core regions may simply be muted by subsequent outbursts. An excellent example of this is J1751+09 (see figure 1) which decays sharply in flux (from $\sim 2.8 \text{ Jy}$ to $\sim 1.0 \text{ Jy}$) between the first two epochs and then rises sharply (from $\sim 1.0 \text{ Jy}$ to $\sim 2.1 \text{ Jy}$) between the last two epochs. These kind of fast fluctuations are examined in §4.1.2.

The fractional decay rates of jet features are smaller with larger projected radius. The exception to this trend is the jet feature in 3C 120 at a mean projected radius of 2 parsecs. This feature rose in flux from 1996.05 to 1996.41 then showed a steady decay over the last four epochs from 1996.41 to 1996.93 with a slope of $(dI/dt)/\langle I \rangle = -0.77 \pm 0.12 \text{ yr}^{-1}$ (see figure 16). The trend of smaller decay rates at larger radii may simply reflect the fact that longer lived features must decay more slowly, or we would not observe them. Figure 17 plots fractional decay rate versus the age of the jet feature, T_{age} . The ages are in our frame and computed by simply dividing the mean angular radius, $\langle R \rangle$, by the proper motion, $\mu = dR/dt$, given in Paper I. For the jet feature in 3C 120 we have plotted the decay slope over the last four epochs with an open triangle. The plot shows a remarkable relation between fractional decay rate, $(dI/dt)/\langle I \rangle$, and the logarithm of T_{age} .

⁷ Of course, when the deviations are taken with respect to mean values, the factor $(n-2)$ in equation 2 should be replaced by $(n-1)$.

⁸ For negative correlations, we make the corresponding δ value negative.

We can construct a simple phenomenological model for the relation in figure 17. If we assume that the flux of a jet feature depends only on its distance along the jet axis, $I \propto R^{-a}$, it follows that the fractional decay rate is inversely proportional to T_{age} :

$$(dI/dt)/I = -a \times (dR/dt)/R = -a/T_{age}. \quad (3)$$

We performed two fits of a generalized version of this model: $(dI/dt)/I = -a/T_{age}^b$, and these fits are plotted in figure 17. The first fit (dashed line) includes all the points for a reduced chi-squared value of 2.2. We noticed that most of the chi-squared was due a single point on 3C 279 with a slightly positive flux slope. The second fit (dotted line) excludes this point for a reduced chi-squared value of 0.9. Both fits find $a = 1.3 \pm 0.1$ and a value of b close to unity.

We note that the jet feature in J2005+77 does not appear in figure 17 because it has no detectable motion (see Paper I), although it does have a very significant flux decay. The simple geometrical model described above cannot account for cases like this, nor can it account for the flux rise seen early in our observations of the jet feature in 3C 120. Another example is the feature in 3C 279, which had a slightly positive (but not significant) flux slope. By the very end of 1997 (a year after the observations presented here), that feature had risen $\sim 50\%$ in flux and dropped in fractional polarization by approximately a factor of two (Homan & Wardle 2000). Many factors can influence the flux evolution of a jet feature in unpredictable ways: variable Doppler factors due to speed or trajectory changes, interactions with the external medium, and catching up with previous slower moving features.

Figure 17 contains eight data points from six different sources, and given the above considerations, it is remarkable that the flux decays fit so well to a simple geometrical model, $I \propto R^{-1.3 \pm 0.1}$. Models of this form have been fit to the flux profiles of VLBI jets by many authors (e.g. Walker, Benson, & Unwin (1987); Unwin & Wehrle (1992); Xu et al. (2000)) with power law indexes typically falling between -1 and -2 , very similar to the power-law index we obtain from the decay rates of superluminal jet features. VLA scale jets also show similar power laws with increasing jet width (presumably proportional to radius) with typical indexes between -1.2 and -1.6 (Bridle & Perley 1984). It is tempting to draw parallels between the physical processes that maintain the brightness of kiloparsec scale jets and those which operate on superluminal jet features. However, we note that selection criteria probably play some role in the range of observed power law indexes, and that in all of these cases, including our measurement from the dynamical decays of jet features, the power law index represents only the mean behavior and averages over a wide range of jet micro-physics (A. H. Bridle, private communication).

4.1.2. Fluctuations in Flux

Figure 18 shows the standard deviation of the correlated fluctuations in flux divided by the mean flux, $\delta I/\langle I \rangle$ (see §3.2), for each core and jet feature plotted against projected radius. Core regions have much larger fractional fluctuations on average than do jet features. In general, core regions with very small projected radii have the largest fluctuations about the linear trends. These core regions have smaller projected radii because they are less biased by nearby, barely resolved jet components which are included in their sum (see §2.4.1).

The fluctuations displayed by core regions fall into three broad categories: (1) a gradual rise and plateau (or fall) in

flux (3C 273, 3C 279, and J1512-09 primarily display this behavior.), (2) sudden, large changes in flux that occur between neighboring epochs (The fluctuations in 3C 120 and J1751+09 are dominated by this behavior.), and (3) smaller epoch to epoch fluctuations (J0530+13 and OJ287 display this behavior). J2005+77 displays the opposite behavior from category (1), with a gentle fall then rise in flux.

The jet feature with the largest fluctuations about the linear trend is U3 (K3) in OJ287. This feature also has a large average flux decay, and the 30% standard deviation is mainly due to a change in the slope of this decay in the middle of our observations. The other jet feature with large fluctuations is U1A+U1B (K1A+K1B) in 3C 120. The flux of this feature rises then decays during our observations as illustrated in figure 16. Beyond a projected radius of 5 pc, no jet feature has fluctuations with a standard deviation larger than 10%, and only one of these, U1 (K1) in J1927+73, is significant. The fluctuations in this component appear to be genuine epoch-to-epoch changes.

4.2. Polarization Variability

Our results for linear trends in polarization and the fluctuations about the linear trends are summarized in tables 5 and 6, and they are plotted and discussed in the following sections.

4.2.1. Linear Trends in Fractional Polarization

Figure 19 plots the linear slopes in fractional polarization over our year long observations against projected radius. As with flux evolution, there are distinct differences between core regions and jet features. Only one core region shows a significant linear trend in fractional polarization, and this is OJ287 with a decay of $3-4\%$ over the year.

Several jet features have significant increases in fractional polarization, and no jet feature shows a significant decrease. This implies that jet features either experience a growth in magnetic field order or emerge from behind Faraday depolarizing screens. Growth in magnetic field order explains most of the increasing fractional polarization observed. We discuss spectral changes, such as changes in any Faraday depolarization, in section 4.3, and with the exception of one feature in 3C 273, we find little evidence of components emerging from behind depolarization screens.

It is interesting that the three jet features at the largest radii have the smallest linear trends in fractional polarization, implying that the degree of magnetic field order changes slowly beyond a projected radius of ~ 10 parsecs.

4.2.2. Fluctuations in Fractional Polarization

Figure 20 shows the standard deviation of the correlated fractional polarization fluctuations for each core and jet feature plotted against projected radius. There are no clear trends or distinct differences between core and jet features. The high point at four percent is the jet component, U3 (K3), in OJ287 which rises and then falls in fractional polarization during our observations.

4.2.3. Linear Trends in Polarization Angle

Figure 21 plots the linear slopes with time of the polarization position angles, χ , of core and jet features. While there are several significant rotations in polarization angle, the core regions of OJ287 and J1512-09 stand out with slopes of -175 and -350 degrees per year respectively.

Figure 22 shows plots of polarization angle versus epoch for the core regions of OJ287 and J1512–09. With such large changes, the $n\pi$ ambiguity in assigning the polarization angles is an issue here. We resolved this ambiguity by simply assigning the angles to give the smallest change between epochs. With this criterion, the only ambiguous case was the jump between epochs 1996.23 and 1996.41 on J1512–09, where the change was less than 90° at 15 GHz and more than 90° at 22 GHz. The choice we made in this case (as displayed in the figure) was consistent with the sign of rotation between the other epochs.

The very large rotations in both of these objects are extremely interesting. Unlike the large polarization angle rotation observed in 3C 120 by Gomez et al. (2000), the rotations are the same at the two frequencies and cannot be due to Faraday effects. The rotations must reflect changes in the observed net magnetic field direction which can be generated either by structural changes in the magnetic field, trajectory changes of a highly polarized sub-component, or changes in flow speed or angle which will change the (aberrated) angle of observation.

The fact that the changes are much larger than 90 degrees rules out opacity effects and simple shock or shear models which would align the magnetic field either perpendicular or parallel to the jet axis. The regular nature of the rotations is very curious, as is the fact that there is no clear relationship between the rotations and either the total intensity or fractional polarization behaviors. The fractional polarization of the core region of OJ287 steadily declines over the last four epochs (during the rotation) from 4% to 2% while the flux has small, irregular, epoch to epoch fluctuations. For J1512–09, the fractional polarization of the core region fluctuates irregularly between 1% and 3% during our observations while the flux shows a single large rise and fall. Although the polarized flux in the core region of J1512–09 falls below our analysis threshold in the final epoch, 1996.93, we note that the 15 GHz polarization image in 1996.93 shows nearly the same polarization angle for the core as the 1996.74 epoch, indicating that the large core rotation had abruptly stopped.

Polarization “rotators” have been observed in integrated polarization observations for over 20 years, e.g. (Ledden & Aller 1979; Altschuler 1980; Aller, Aller, & Hodge 1980). The acceleration-aberration model of Blandford & Konigl (1979) can not account for rotations larger than 180 degrees, and either a true physical rotation or a quasi-circular motion of the emitting region seems to be at work (Aller, Hodge, & Aller 1981). Jones et al. (1985) interpreted observations of polarization rotations in terms of a random walk model when the magnetic field evolution is dominated by turbulence. More recently, Hughes, Aller, & Aller (1998) performed a wavelet analysis on two decades of UMRAO observations of OJ287. Their observations were not consistent with the random walk model, and the analysis suggested a small amplitude, cyclic fluctuation in the flow direction. Our observations cannot easily distinguish between these models, but they do provide some constraints. The rotations we observed occurred in the compact core region ($\lesssim 0.3$ pc, in projection). As noted above, the rotations were large ($\gtrsim 180^\circ$) and had no clear relation with the flux and fractional polarization evolution of the core region. Additionally, the observed rotations are *not* seen in the integrated UMRAO monitoring observations that accompany our VLBI observations. In the integrated measurements, these rotations

are muted by contributions from polarized jet features, suggesting that polarization rotations may be even more common than previously revealed by integrated monitoring.

We noted above that these two large polarization angle rotations cannot be due to Faraday rotation as they have the same magnitude at both frequencies. The following analysis of polarization rotations observed in jet features is made with the assumption that changes in the net magnetic field direction primarily drive all of the polarization angle changes we observe. This assumption is supported in section 4.2.5.

It is interesting to examine the relationship between the linear trends in polarization angle and the alignment with the structural position angle of the jet feature, θ . Panel (a) of figure 23 shows polarization angle rotation as a function of the difference between the mean polarization angle and the mean structural position angle. In this plot, a positive slope indicates a rotation of the polarization angle such as to align the magnetic field more closely with the mean structural position angle, and a negative slope indicates a rotation away from magnetic field alignment.⁹ It is interesting that both $\geq 3\sigma$ slopes and two of three $\geq 2\sigma$ slopes are in the direction of aligning the magnetic field along the jet axis (assumed to be parallel to the mean structural position angle).

Panel (b) of figure 23 plots fractional polarization slope against the same $|\langle\chi\rangle - \langle\theta\rangle|$ axis as in panel (a). As discussed in section 4.2.1, the only significant linear trends we see in the fractional polarizations of jet features are increases with time. With the possible exception of a jet feature from 3C 273, we believe the positive slopes reflected increasing magnetic field order in jet features. Taken with the observation from panel (a) that the magnetic field of jet features tends to rotate in the direction of alignment with the jet axis, we have a tentative picture suggesting increasing longitudinal field order, which is (1) produced in the jet features themselves as they propagate, perhaps through shear, and/or (2) part of the underlying flow which is sampled (and enhanced) by the passing jet features.

While the above picture regarding increasing longitudinal field in the jets is attractive, we note that in only one jet feature (U1A+U1B in 3C 120) do we clearly observe *both* an increase in magnetic field order and a rotation towards magnetic field alignment with the jet axis. (Gomez, Marscher, & Alberdi (1999) observe qualitatively the same behavior in two subsequent jet features, their F and G, in 3C 120.) We also note that our sample of jet features is dominated by magnetic fields within 45° of alignment with the jet axis; a collection of jet features with magnetic fields oriented at larger (“shock-like”) angles to the jet axis might behave quite differently. At 5 GHz, Cawthorne et al. (1993) found a trend of increasing longitudinal magnetic field order with jet radius in quasars, which tended to have magnetic fields aligned with the jet axis. They found this trend by plotting single epoch observations of many sources on one plot. Here we find a similar result by observing the dynamic evolution of the magnetic field of individual jet features.

4.2.4. Fluctuations in Polarization Angle

Figure 24 plots the standard deviation of the correlated polarization angle fluctuations against projected radius (panel a) and mean fractional polarization (panel b). While we see very little relationship with projected radius, the polarization angle fluctuations are smaller with larger fractional polarization. This

⁹ In the absence of strong Faraday effects the polarization position angle for synchrotron radiation is perpendicular to the net magnetic field direction assuming the optical depth is $\lesssim 7$.

may imply that polarization angle fluctuations are generated by relatively small scale orderings or re-orderings of the magnetic field. For highly polarized components, such small scale changes would have little effect on the net polarization angle direction.

4.2.5. Are Polarization Angle Changes due to Faraday Rotation?

We evaluate this question by plotting the ratio of the polarization angle changes at 15 GHz to those at 22 GHz in figure 25. If Faraday rotation is primarily responsible for the changes we observe, the changes at 15 GHz should be 2.1 times those at 22 GHz. Panel (a) of figure 25 plots the linear slope ratio, and panel (b) plots the ratio of the RMS fluctuations. Low signal to noise points have been filtered out by only plotting features with a mean slope of greater than 2σ significance in panel (a) and by only plotting features where the fluctuations are correlated at the $r > 0.5$ level in panel (b). While there is still some scatter in the plots, the data clearly cluster around ratios of 1.0 rather than 2.1. A ratio of 1.0 is precisely what we expect if the observed polarization angle changes reflect changes in the net magnetic field direction.

We can investigate this further by examining the mean position angle difference, $\langle \Delta\chi \rangle$, between frequencies in table 7, and we see little evidence for large mean Faraday rotations in the core regions and jet features we follow. The difference between the two frequencies is typically a few degrees with error bars comparable to or larger than the difference. These results are consistent with Taylor (1998, 2000) who finds observed rotation measures of ~ 1000 rad/m 2 ($\Delta\chi_{15-22} \approx 10^\circ$) for quasars cores and falling off to < 100 rad/m 2 ($\Delta\chi_{15-22} \lesssim 1^\circ$) beyond a projected radius of 20 pc. Rotation measures affecting individual features would need to change by $\geq 100\%$ (in several cases many times this amount) in less than a year to explain the significant polarization angle changes that we observe. Zavala & Taylor (2001) recently reported a change of 800 rad/m 2 over 1.5 years in the core of 3C 279; they also observed spatial variations spanning 4000 rad/m 2 in the inner 10 pc of 3C 273.

While large rotation measure changes are possible, particularly in AGN cores, we do not find evidence that such variability in the Faraday screens is responsible for the polarization angle changes that we observe. In general, the polarization angle changes are the same magnitude at both frequencies, and are best explained by changes in the net magnetic field direction. In examining the data for individual features in detail, no case stands out as having significant polarization angle changes driven by Faraday rotation, although we cannot Faraday rotation as the cause in a few cases.

4.3. Spectral Variability

Table 7 lists average spectral properties (spectral index, α , polarization ratio, m_{ratio} , and polarization angle difference, $\Delta\chi$) and their respective linear slopes with time over our year-long window of observation. Here we are primarily interested in the spectral evolution of core and jet features as revealed by these linear slopes.

All of the $\geq 3\sigma$ slopes are in spectral index. The core regions of 3C 273 and 3C 279 both have a negative spectral index slope indicating a shift towards more optically thin radiation. Both of these core regions undergo outbursts during our observations with a distinct rise and plateau (with perhaps a small fall) in total core flux, and in both cases we clearly see the development of new jet components in the core region (see Paper I). In

3C 273 the spectral changes in the core are linked with the sudden appearance of circular polarization in the middle of 1996 (Homan & Wardle 1999).

The core regions of J1751+09 and J2005+77 have distinctly positive spectral index slopes indicating a shift towards more optically thick radiation. Both of these core regions show a flux dip early in our year-long window of observations followed by a rise in flux at the end of the year. In J1751+09, both dip and rise occur sharply as discussed in §4.1.2, and in J2005+77 the dip and rise are more gradual. The shift towards higher optical depth may be connected with particle injection at the start of a new outburst. Together with the observations of 3C 273 and 3C 279, we may be seeing different phases of a single outburst/component ejection cycle (e.g. (Valtaoja, Lähteenmäki, Teräsranta, & Lainela 1999)) similar to that observed in UMRAO single dish monitoring (Aller, Aller, & Hughes 1996) with a shift towards higher opacity very early in the cycle as the outburst is developing and a shift towards lower opacity as the outburst peaks and a new component is ejected.

We also see a positive spectral index slope in the jet feature U1 (K1) of J1927+73. In the same source we detect a similar positive slope at the 2.3σ level on the nearby component U2 (K2). These two components are nearly side by side in the jet and move on radial trajectories (see Paper I). Their simultaneous shift towards flatter spectral index may be related to passing through local jet conditions such as a mild standing shock where particle re-acceleration is occurring. It is interesting to note that the feature U1 (K1) also has significant $\sim 10\%$ fluctuations in its flux.

While there are no $\geq 3\sigma$ slopes (and only two $\geq 2\sigma$) in either fractional polarization ratio or polarization angle difference between the frequencies, there are two individual variability events in fractional polarization that are interesting to consider. The first is on the jet feature U9+U8+U7 in 3C 273, and figure 26 shows fractional polarization at both 15 and 22 GHz plotted against epoch. The fractional polarization ratio makes a distinct shift in the middle of the observations from being strongly depolarized at 15 GHz relative to 22 GHz to having roughly equal amounts of polarization at the two frequencies. The fractional polarization of this feature increases continually during our observations, and a more detailed examination of sub-component behavior leads us to believe that much of the fractional polarization increase in this feature is due to emergence from behind a Faraday depolarizing screen (J. F. C. Wardle et al., in preparation). We do not see similar evidence for emergence from behind Faraday depolarizing screens in other jet features.

Jet feature U1A+U1B (K1A+K1B) in 3C 120 also has interesting fractional polarization changes between 15 and 22 GHz, and its' fractional polarization over time is plotted in figure 27. After the second epoch, we observe a distinct separation in the fractional polarization at the two frequencies with fractional polarization at 15 GHz being noticeably *larger*. Interestingly, the two frequencies track one another in the jump in fractional polarization from epochs 1996.57 to 1996.74. The higher levels of polarization at 15 GHz are clearly visible in our maps as well as our model-fits, and cannot be explained by traditional Faraday depolarization which would have less fractional polarization at 15 GHz. Satisfactory explanations for the observed effect require at least a two component model, such as a spine-sheath structure, where one component has a more highly ordered field and a steeper spectral index. The required difference in spectral index between sub-components is large if the two components

have similar polarizations or even if one of the components is unpolarized. We can reduce the required spectral index difference considerably if the two sub-components have significant polarization cancellation between them. In §4.2.3 we noted this jet feature showed both an increase in fractional polarization and a rotation of the polarization angle indicating increasing magnetic field order along the jet axis. Perhaps we are seeing an increasing contribution from ordered magnetic field in a shear layer which has a distinctly steeper spectrum than the bulk of the jet.

5. SUMMARY

We have analyzed the flux and polarization evolution of twelve parsec-scale radio jets over a single year. These objects were monitored with the VLBA at 15 and 22 GHz for six epochs, spaced at approximately two month intervals, during 1996. We analyzed the flux, fractional polarization, and polarization position angle behavior of both core regions and jet features. Our analysis considered both the linear trends of these quantities with time and the fluctuations about the linear trends. With dual observing frequencies, we were able to examine spectral trends and distinguish between Faraday effects and changes in the net magnetic field directions of core regions and jet features. The closely spaced frequencies were also extremely helpful in assessing the reality of the fluctuations we observed.

The key results of our analysis include the following:

(1) Jet features generally decayed in flux, with older features decaying more slowly than younger features. There was a distinct relation between the age of a feature, as measured by its position and proper motion, and its rate of flux decay. We found that this relationship could be explained if the flux of a jet feature depended only upon its position in the jet: $I \propto R^{-1.3 \pm 0.1}$. (We note that at least one jet feature did show significant brightening between some epochs, and another jet feature had a significant flux decay with no apparent proper motion.)

(2) We observed significant fluctuations in the flux of both core regions and jet features. Core regions tended to have larger fractional fluctuations than jet features, with more compact core regions having larger fluctuations.

(3) Jet features either had a significant increase in fractional polarization or showed no change, with the smallest changes in the features at the largest projected radii. With the exception of a single jet feature (U9+U8+U7 in 3C 273), we saw no evidence for features emerging from behind Faraday depolarizing screens, and increasing magnetic field order explains most of the increasing fractional polarization we observed.

(4) Changes in the net magnetic field direction were the primary cause of the polarization angle changes we observed. The linear rotations and fluctuations in polarization angle were of the same size at 15 and 22 GHz, and could not easily be explained by Faraday rotation which would have required the changes at 15 GHz to be twice the size of the changes at 22

GHz.

(5) We observed large ($\gtrsim 180^\circ$) rotations in the polarization position angles of two core regions. These rotations were the same at both observing frequencies and could not be due to Faraday effects. The rotations were similar to those that have been observed in integrated measurements for over twenty years, and we could not easily distinguish between previously proposed models for this phenomenon.

(6) The magnetic field of jet features tended to become increasingly longitudinal. Four out of five polarization angle rotations were in the direction of aligning the magnetic field with the jet axis. This observation, coupled with the tendency towards increasing magnetic field order described above, suggests increasing longitudinal field order. However, we note that we clearly observed *both* a rotation towards alignment and increasing field order in only one jet feature, U1A+U1B in 3C 120. In this feature there was also an interesting “negative depolarization” effect with 15 GHz more highly polarized than 22 GHz, suggesting an increasing contribution from a longitudinally ordered field in a shear layer that has a steeper spectral index than the bulk of the flow.

(7) Polarization angle fluctuations decrease in amplitude with increasing fractional polarization. Features with more highly ordered magnetic fields would be less affected by small scale orderings or re-orderings of the field which might have driven the polarization angle fluctuations.

(8) We observed significant spectral index trends in the core regions of four sources and in the jet features of one object. For the core regions, the spectral index moved towards more optically thin radiation as core outbursts in two sources came to a peak and plateaued (or declined slightly), and in two other sources the spectral index moved towards more optically thick radiation in the gap between outbursts. In the jet of J1927+73, there was a shift to flatter spectral indexes in two features that are moving side-by-side in the jet on nearly parallel tracks. These features may have experienced the same local conditions in the jet, such as a mild standing shock where particle re-acceleration was occurring.

6. ACKNOWLEDGMENTS

This work has been supported by NASA Grants NGT-51658 and NGT5-50136 and NSF Grants AST 91-22282, AST 92-24848, AST 94-21979, AST 95-29228, AST 98-02708, and AST 99-00723. We thank C. C. Cheung and G. Sivakoff for their assistance in the initial organization of the modelfit data, and Alan Bridle for helpful discussion regarding jet flux profiles. This research has made use of the NASA/IPAC Extragalactic Database (NED) which is operated by the Jet Propulsion Laboratory, California Institute of Technology, under contract with the National Aeronautics and Space Administration. This research has also made use of NASA’s Astrophysics Data System Abstract Service.

APPENDIX

EMPIRICAL ESTIMATES OF THE UNCERTAINTIES IN MEASURING VLBI COMPONENT PROPERTIES

In section 3 we discussed the difficulties in deducing robust “1 σ ” uncertainty estimates for the fluxes and polarizations of core and jet features observed in VLBI jets. Lack of good a-priori uncertainty estimates led us to correlate observed fluctuations about the linear trends between our two observing bands (15 and 22 GHz), as described in §3.2, to assess the reality of these fluctuations. In this appendix, we take the methods in §3.2 a step further to obtain empirical estimates of the uncertainties in measuring VLBI component properties.

Here we are interested in the un-correlated part of the fluctuations discussed in §3.2.

$$\Omega_{15} = (1-r) \times \frac{\sum_i \Delta_{15i}^2}{n-2} \quad \Omega_{22} = (1-r) \times \frac{\sum_i \Delta_{22i}^2}{n-2}. \quad (\text{A1})$$

Note that these expressions are very similar to equation 2 with r replaced by $(1-r)$, so here Ω is the *un-correlated* part of the variance of the deviations at each frequency. For negative values of r , we set $r = 0$ for the purposes of this calculation. The square-root of Ω gives the standard deviation of the un-correlated fluctuations, and we have computed this for each quantity and frequency: $\sigma I_{15} = \sqrt{\Omega_{15}}$, etc. We used the second Monte Carlo simulation described in §3.2 to place rough uncertainties on these σ values. Table 8 presents these numbers for each core and jet feature appearing in our analysis.

These un-correlated fluctuations consist of (1) real spectral changes in core and jet feature properties, and (2) any measurement, calibration, *and* model-fitting errors that are not systematic between epoch or frequency. Because we have no way of separating out the real spectral changes, we take these estimates of the standard deviation of the un-correlated fluctuations as conservative estimates on the total (non-systematic) uncertainty in measuring VLBI flux and polarization of core and jet features in a single epoch.

Figures 28–30 plot these uncertainty estimates against projected radius for each quantity at both frequencies. For I at 15 GHz most features have an estimated uncertainty of less than 5% in a single epoch, with several particularly good cases of 2–3% and a few poorer cases of $\sim 10\%$. For I at 22 GHz, 5% or better is the case for some of the more extended core regions (where nearby jet components have been summed into the core flux), but 5–10% is more typical for jet features with a couple cases approaching 20%. For fractional polarization, 0.5% is typical at 15 GHz, and 0.5–1.0% is typical at 22 GHz. For polarization angle, uncertainties $\leq 5^\circ$ are typical at both frequencies with best case values $\leq 2^\circ$ and worse case values up to $\sim 10^\circ$.

REFERENCES

Aller, H. D., Aller, M. F., Latimer, G. E., & Hodge, P. E. 1985 *ApJS*, 59, 513
 Aller, H. D., Aller, M. F., & Hodge, P. E. 1981 *AJ*, 86, 325
 Aller, H. D., Hodge, P. E., & Aller, M. F. 1981 *ApJ*, 248, L5
 Aller, M. F., Aller, H. D., & Hughes, P. A. 1996, in *ASP Conf. Ser.* 110, eds. H. R. Miller, J. R. Webb, & J. C. Noble, 193
 Aller, M. F., Aller, H. D., Hughes, P. A., & Latimer, G. E. 1999 *ApJ*, 512, 601
 Altschuler, D. R. 1980 *AJ*, 85, 1559
 Blandford, R. D., & Konigl, A. 1979 *ApJ*, 232, 34
 Bridle, A. H., & Greisen, E. W. 1994 *AIPS Memo* 87
 Bridle, A. H., & Perley, R. A. 1984 *ARA&A*, 22, 319
 Brown, L. F., Roberts, D. H., & Wardle, J. F. C. 1994 *ApJ*, 437, 108
 Cawthorne, T. V., Wardle, J. F. C., Roberts, D. H., & Gabuzda, D. C. 1993 *ApJ*, 416, 519
 Cotton, W. D. 1993 *AJ*, 106, 1241
 Gomez, J., Marscher, A. P., Alberdi, A., Jorstad, S. G., & Garcia-Miro C. 2000 *Science*, 289, 2317
 Gomez, J., Marscher, A. P., & Alberdi, A. 1999 *ApJ*, 521, L29
 Greisen, E. W. 1988 *AIPS Memo* 61
 Homan, D. C., Ojha, R., Wardle, J. F. C., Roberts, D. H., Aller, M. F., Aller, H. D., & Hughes, P. A. 2001 *ApJ*, 549, 840
 Homan, D. C., & Wardle, J. F. C. 1999 *AJ*, 118, 1942
 Homan, D. C., & Wardle, J. F. C. 2000 *ApJ*, 535, 575
 Hughes, P. A., Aller, H. D., & Aller, M. F. 1998 *ApJ*, 503, 662
 Jones, T. W., Rudnick, L., Aller, H. D., Aller, M. F., Hodge, P. E., & Fiedler, R. L. 1985 *ApJ*, 290, 627
 Ledden, J. E., & Aller, H. D. 1979, *ApJ*, 229, L1
 Leppänen, K. J., Zensus, J. A., & Diamond, P. J. 1995 *AJ*, 110, 2479
 Lobanov, A. P., & Zensus, J. A. (1999) *ApJ*, 521, 509
 Napier, P. J. 1995 in *ASP Conf. Ser.* 82, *Very Long Baseline Interferometry with the VLBA*, ed. Zensus, J. A., Diamond, P. J., & Napier, P. J., 57
 Press, W. H., Teukolsky, S. A., Vetterling, W. T., & Flannery, B. P. 1995, *Numerical Recipes in C*, (Cambridge University Press) p. 681.
 Roberts, D. H., Wardle, J. F. C., & Brown, L. F. 1994, *ApJ*, 427, 718
 Shepherd, M. C., Pearson, T. J., & Taylor, G. B. 1994 *BAAS*, 26, 987
 Shepherd, M. C., Pearson, T. J., & Taylor, G. B. 1995 *BAAS*, 27, 903
 Taylor, G. B. 1998 *ApJ*, 506, 637
 Taylor, G. B. 2000 *ApJ*, 533, 95
 Thompson, A. R. 1995 in *ASP Conf. Ser.* 82, *Very Long Baseline Interferometry with the VLBA*, ed. Zensus, J. A., Diamond, P. J., & Napier, P. J., 73
 Unwin, S. C., Cohen, M. H., Biretta, J. A., Pearson, T. J., Seielstad, G. A., Walker, R. C., Simon, R. S., & Linfield, R. P. 1985 *ApJ*, 289, 109
 Unwin, S. C., & Wehrle, A. E. 1992 *ApJ*, 398, 74
 Valtaoja, E., Lähteenmäki, A., Teräsranta, H., & Lainela, M. 1999, *ApJS*, 120, 95
 Vermeulen, R. C., & Cohen, M. H. 1994 *ApJ*, 430, 467
 Walker, R. C., Benson, J. M., & Unwin, S. C. 1987 *ApJ*, 316, 546
 Wardle, J. F. C., Homan, D. C., Ojha, R., & Roberts, D. H. 1998 *Nature*, 395, 457
 Wehrle, A. E. et al. 1992 *ApJ*, 391, 589
 Xu, C., Baum, S. A., O'Dea, C. P., Wrobel, J. M., & Condon, J. J. 2000 *AJ*, 120, 2950
 Zavala, R. T., & Taylor, G. B. 2001 *ApJ*, 550, L47

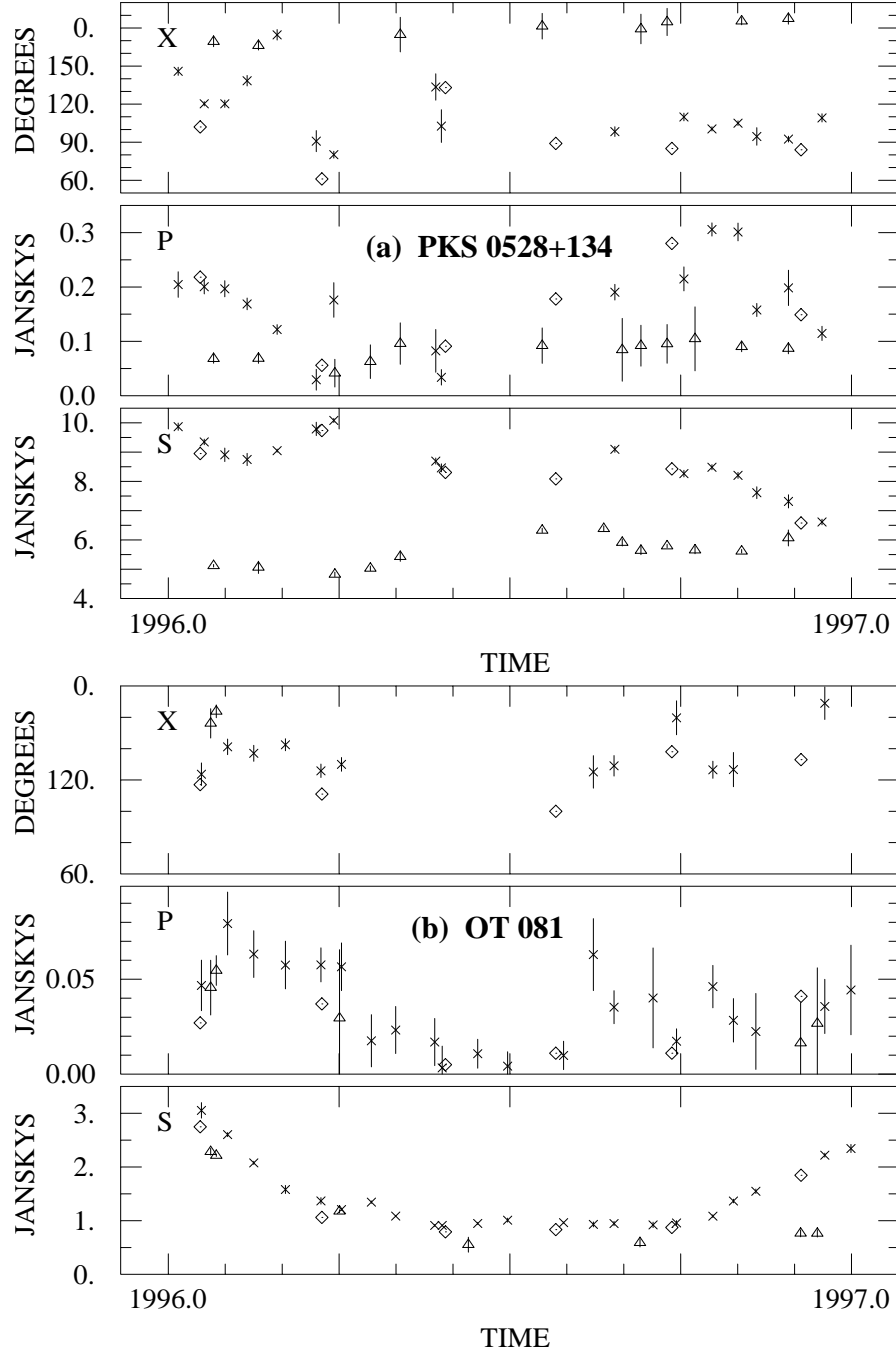


FIG. 1.— Comparison of single dish monitoring by the UMRAO at 14.5 GHz (\times symbols) to the integrated VLBI results at 15 GHz (open diamonds). Total intensity (I), polarized intensity (P), and polarization position angle (X) are plotted for two compact sources, PKS 0528+134 (J0530+14) in panel (a), and OT 081 (J1751+09) in panel (b). UMRAO 5 GHz results (open triangles) are included to illustrate opacity effects.

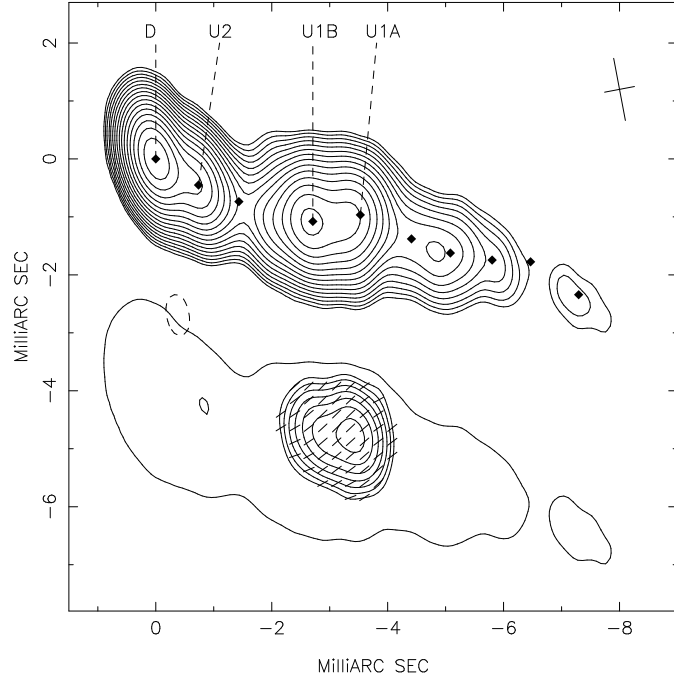


FIG. 2.— Total intensity and polarization images of 3C 120 in epoch 1996.57 at 15 GHz. The total intensity map has a peak flux of 0.73 Jy/beam with contour levels starting at 0.003 Jy/beam and increasing in steps of $\times\sqrt{2}$. The polarization image has a peak flux of 0.029 Jy/beam with contour levels starting at 0.003 Jy/beam and increasing in steps of $\times\sqrt{2}$. Tick marks represent the polarization position angle. A single I contour is drawn around the P to show registration. For variability analysis, we consider two jet features: (1) the core region, consisting of the components D+U2 (D+K3+K2 at 22 GHz), and (2) the strong jet feature consisting of U1A+U1B (K1A+K1B). This feature moves with a mean apparent speed of 4.3 times the speed of light (Paper I);

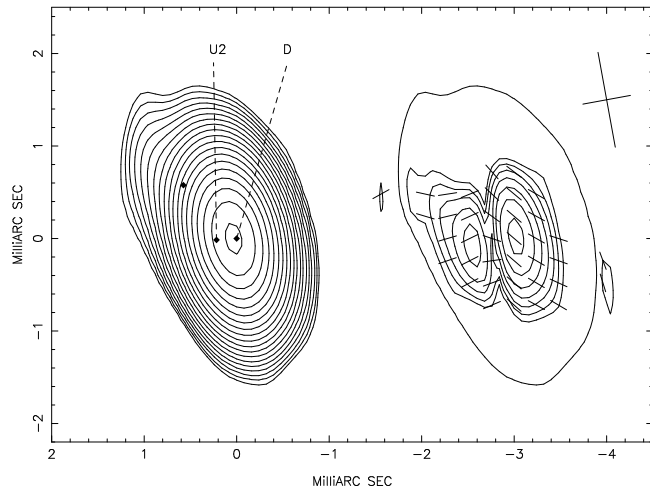


FIG. 3.— Total intensity and polarization images of J0530+13 in epoch 1996.23 at 15 GHz. The total intensity map has a peak flux of 8.20 Jy/beam with contour levels starting at 0.015 Jy/beam and increasing in steps of $\times\sqrt{2}$. The polarization image has a peak flux of 0.071 Jy/beam with contour levels starting at 0.008 Jy/beam and increasing in steps of $\times\sqrt{2}$. Tick marks represent the polarization position angle. A single I contour is drawn around the P to show registration. For variability analysis, we consider only the core region, consisting of D+U2 (D+K2 at 22 GHz). The competing polarizations of D and U2 (K2) are the most distinct in the displayed epoch.

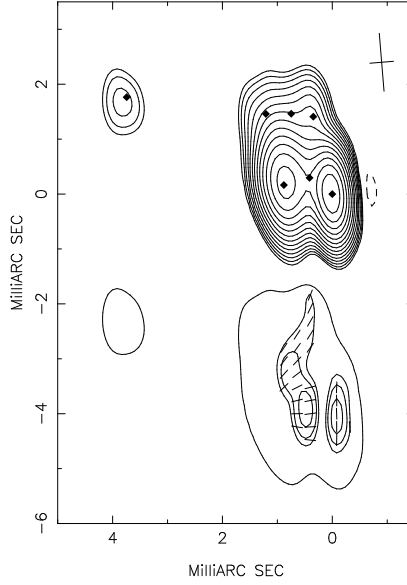


FIG. 4.— Total intensity and polarization images of J0738+73 in epoch 1996.74 at 15 GHz. The total intensity map has a peak flux of 0.37 Jy/beam with contour levels starting at 0.003 Jy/beam and increasing in steps of $\times\sqrt{2}$. The polarization image has a peak flux of 0.007 Jy/beam with contour levels starting at 0.003 Jy/beam and increasing in steps of $\times\sqrt{2}$. Tick marks represent the polarization position angle. A single I contour is drawn around the P to show registration. The jet core is the western-most feature with jet components extending over a range of position angles to the east. This was a difficult source to model consistently across epoch and frequency. For this reason, we have simply summed the entire list of model components and analyze the variability of their total.

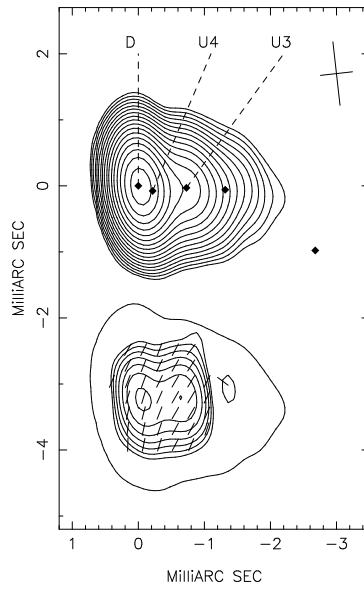


FIG. 5.— Total intensity and polarization images of OJ287 in epoch 1996.57 at 15 GHz. The total intensity map has a peak flux of 0.96 Jy/beam with contour levels starting at 0.003 Jy/beam and increasing in steps of $\times\sqrt{2}$. The polarization image has a peak flux of 0.026 Jy/beam with contour levels starting at 0.003 Jy/beam and increasing in steps of $\times\sqrt{2}$. Tick marks represent the polarization position angle. A single I contour is drawn around the P to show registration. For variability analysis, we consider two features: (1) the core region consisting of D+U4 (D+K4 at 22 GHz), and (2) the jet component U3 (K3), which originates very near the core and moves rapidly outward during our observations, $\beta_{app} = 19$ (Paper I).

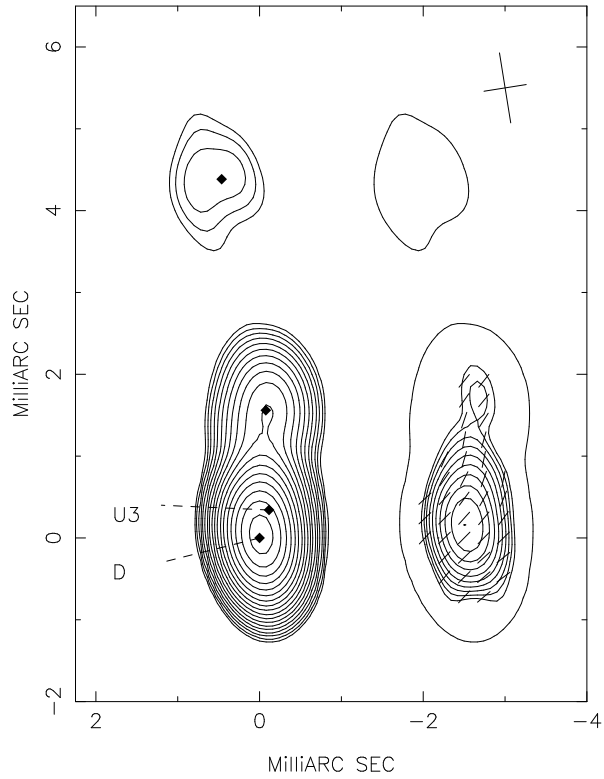


FIG. 6.— Total intensity and polarization images of J1224+21 in epoch 1996.57 at 15 GHz. The total intensity map has a peak flux of 1.31 Jy/beam with contour levels starting at 0.003 Jy/beam and increasing in steps of $\times\sqrt{2}$. The polarization image has a peak flux of 0.068 Jy/beam with contour levels starting at 0.003 Jy/beam and increasing in steps of $\times\sqrt{2}$. Tick marks represent the polarization position angle. A single I contour is drawn around the P to show registration. This source is observed at only five epochs, and we are able to reliably track only the core region, consisting of D+U3 (D+K4+K3 at 22 GHz), for variability analysis.

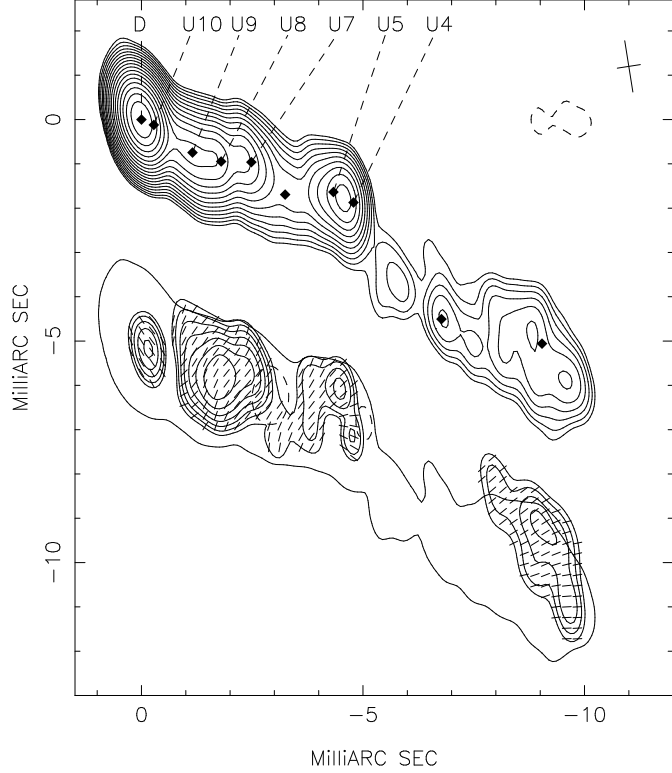


FIG. 7.— Total intensity and polarization images of 3C 273 in epoch 1996.57 at 15 GHz. The total intensity map has a peak flux of 10.68 Jy/beam with contour levels starting at 0.030 Jy/beam and increasing in steps of $\times\sqrt{2}$. The polarization image has a peak flux of 0.166 Jy/beam with contour levels starting at 0.015 Jy/beam and increasing in steps of $\times\sqrt{2}$. Tick marks represent the polarization position angle. A single I contour is drawn around the P to show registration. For variability analysis, we consider three features: (1) the core region, consisting of D+U10 (D+K10 at 22 GHz), (2) the first jet region, consisting of U9+U8+U7 (K9+K8+K7), and (3) the bright jet knot, consisting of U5+U4 (K5+K4). Both jet features move with apparent speeds of approximately 10 times the speed of light (Paper I).

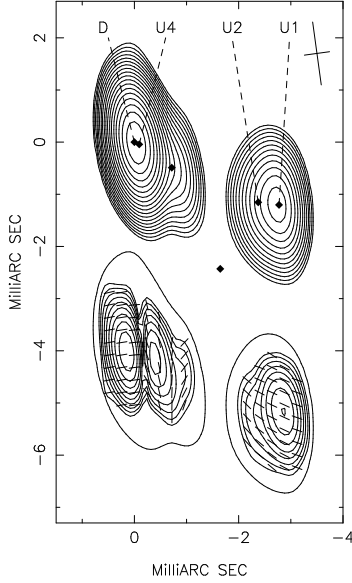


FIG. 8.— Total intensity and polarization images of 3C 279 in epoch 1996.41 at 15 GHz. The total intensity map has a peak flux of 14.71 Jy/beam with contour levels starting at 0.030 Jy/beam and increasing in steps of $\times\sqrt{2}$. The polarization image has a peak flux of 0.317 Jy/beam with contour levels starting at 0.015 Jy/beam and increasing in steps of $\times\sqrt{2}$. Tick marks represent the polarization position angle. A single I contour is drawn around the P to show registration. For variability analysis, we follow the core region, D+U4 (D+K4 at 22 GHz), and the strong jet feature, U2+U1 (K2+K1) which moves at $\beta_{app} = 7.6$ (see Paper I). The competing polarizations of D and U4 are the most distinct in the displayed epoch.

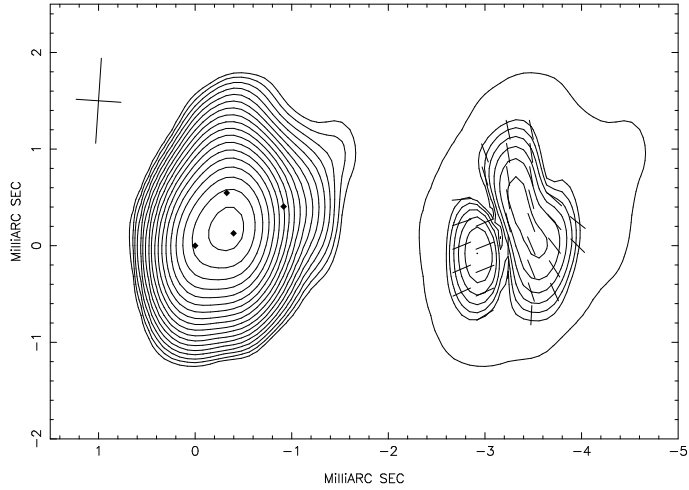


FIG. 9.— Total intensity and polarization images of J1310+32 in epoch 1996.41 at 15 GHz. The total intensity map has a peak flux of 1.70 Jy/beam with contour levels starting at 0.004 Jy/beam and increasing in steps of $\times\sqrt{2}$. The polarization image has a peak flux of 0.026 Jy/beam with contour levels starting at 0.004 Jy/beam and increasing in steps of $\times\sqrt{2}$. Tick marks represent the polarization position angle. A single I contour is drawn around the P to show registration. For variability analysis, we have simply summed all the VLBI model components.

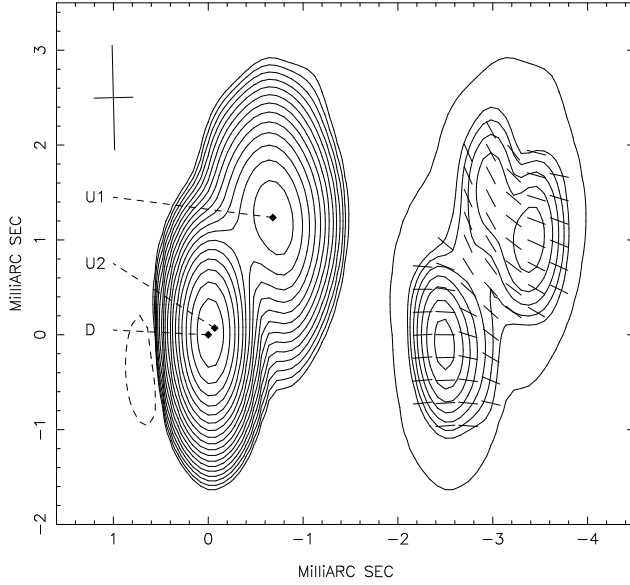


FIG. 10.— Total intensity and polarization images of J1512-09 in epoch 1996.41 at 15 GHz. The total intensity map has a peak flux of 1.46 Jy/beam with contour levels starting at 0.003 Jy/beam and increasing in steps of $\times\sqrt{2}$. The polarization image has a peak flux of 0.028 Jy/beam with contour levels starting at 0.003 Jy/beam and increasing in steps of $\times\sqrt{2}$. Tick marks represent the polarization position angle. A single I contour is drawn around the P to show registration. For variability analysis, we consider two features: (1) the core region consisting of $D+U2$ ($D+K2$ at 22 GHz), and (2) the jet component $U1$ ($K1$) which has a proper motion of $\beta_{app} = 21$ (Paper I).

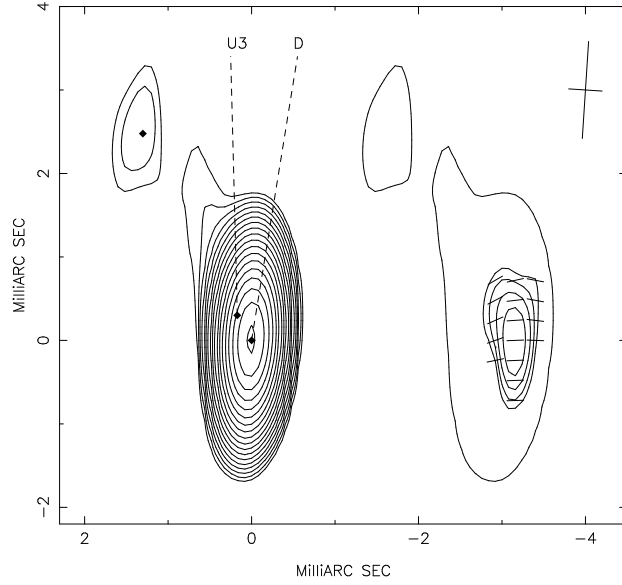


FIG. 11.— Total intensity and polarization images of J1751+09 in epoch 1996.57 at 15 GHz. The total intensity map has a peak flux of 0.77 Jy/beam with contour levels starting at 0.002 Jy/beam and increasing in steps of $\times\sqrt{2}$. The polarization image has a peak flux of 0.012 Jy/beam with contour levels starting at 0.003 Jy/beam and increasing in steps of $\times\sqrt{2}$. Tick marks represent the polarization position angle. A single I contour is drawn around the P to show registration. For variability analysis, we consider only the core region, $D+U3$ (D at 22 GHz).

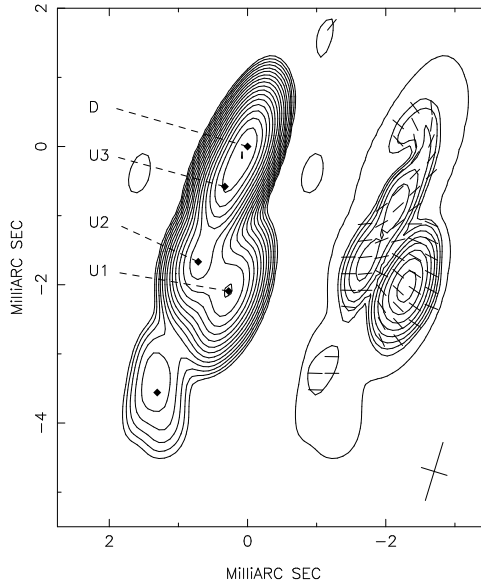


FIG. 12.— Total intensity and polarization images of J1927+73 in epoch 1996.57 at 15 GHz. The total intensity map has a peak flux of 1.46 Jy/beam with contour levels starting at 0.004 Jy/beam and increasing in steps of $\times\sqrt{2}$. The polarization image has a peak flux of 0.040 Jy/beam with contour levels starting at 0.003 Jy/beam and increasing in steps of $\times\sqrt{2}$. Tick marks represent the polarization position angle. A single I contour is drawn around the P to show registration. For variability analysis, we consider three features: (1) the core region consisting of $D+U3$ ($D+K3$ at 22 GHz), (2) the first jet component $U2$ ($K2$), and (3) the second jet component $U1$ ($K1$). These two jet features travel on radial trajectories with apparent speeds of approximately 4–5 times the speed of light (Paper I).

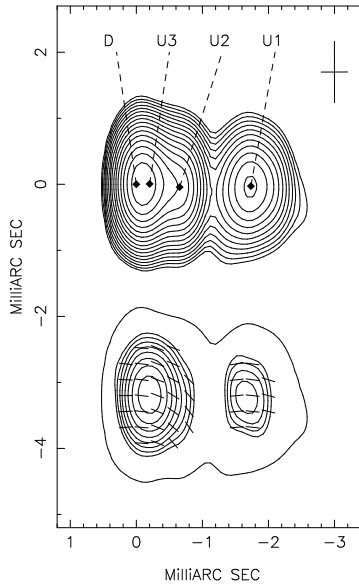


FIG. 13.— Total intensity and polarization images of J2005+77 in epoch 1996.23 at 15 GHz. The total intensity map has a peak flux of 0.51 Jy/beam with contour levels starting at 0.002 Jy/beam and increasing in steps of $\times\sqrt{2}$. The polarization image has a peak flux of 0.029 Jy/beam with contour levels starting at 0.002 Jy/beam and increasing in steps of $\times\sqrt{2}$. Tick marks represent the polarization position angle. A single I contour is drawn around the P to show registration. For variability analysis, we consider two features: (1) the core region, $D+U3+U2$ ($D+K2$ at 22 GHz), and (2) the jet component $U1$ ($K1$), which doesn't move during our observations (Paper I).

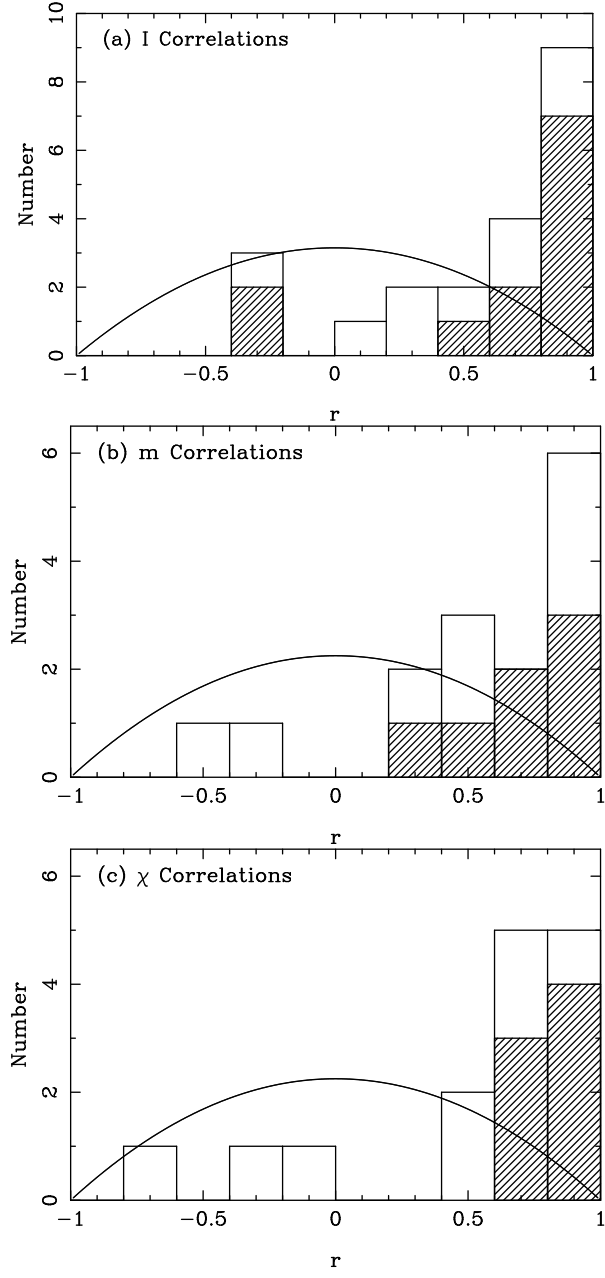


FIG. 14.— Histograms of the correlation, r , between the fluctuations at 15 and 22 GHz in total intensity (panel (a)), fractional polarization (panel (b)), and polarization position angle (panel (c)). Jet features are represented by empty bars, and hash-filled bars represent core features. The solid lines approximate the expected distributions if there were no intrinsic correlation between the fluctuations at 15 and 22 GHz. The large excess of positive correlations shows that real, short term ($\lesssim 0.5$ yr) fluctuations are common throughout our data set.

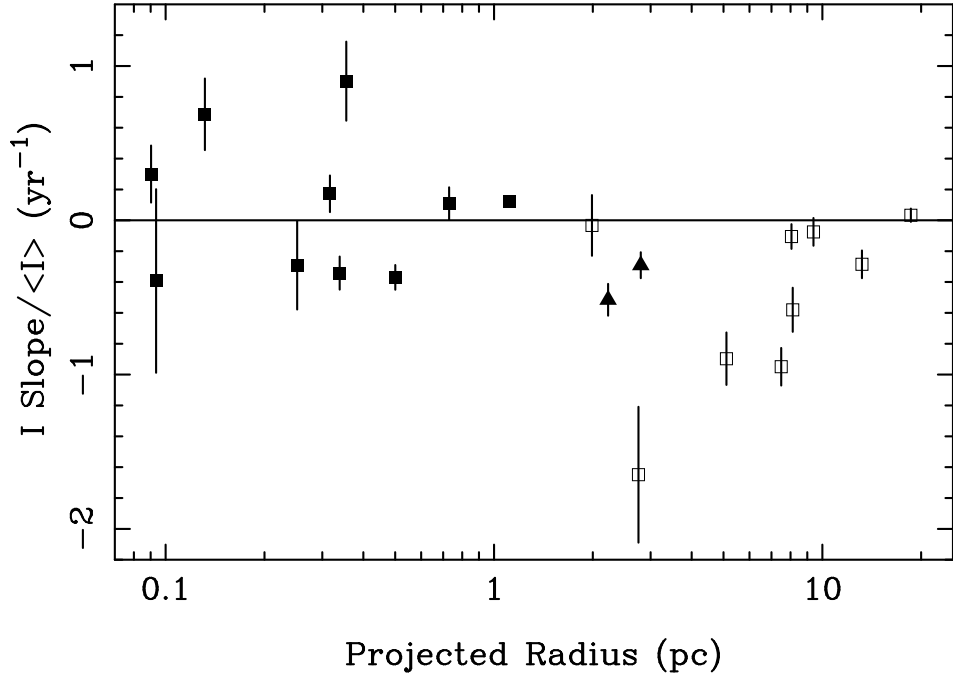


FIG. 15.—Fractional flux slope, $\langle \dot{I}/\langle I \rangle \rangle$ (see table 4), plotted against projected radius in parsecs. Filled squares represent core regions, and open squares represent jet features. J0738+17 and J1312+32, where we have analyzed the total VLBI flux of the source, are represented by filled triangles.

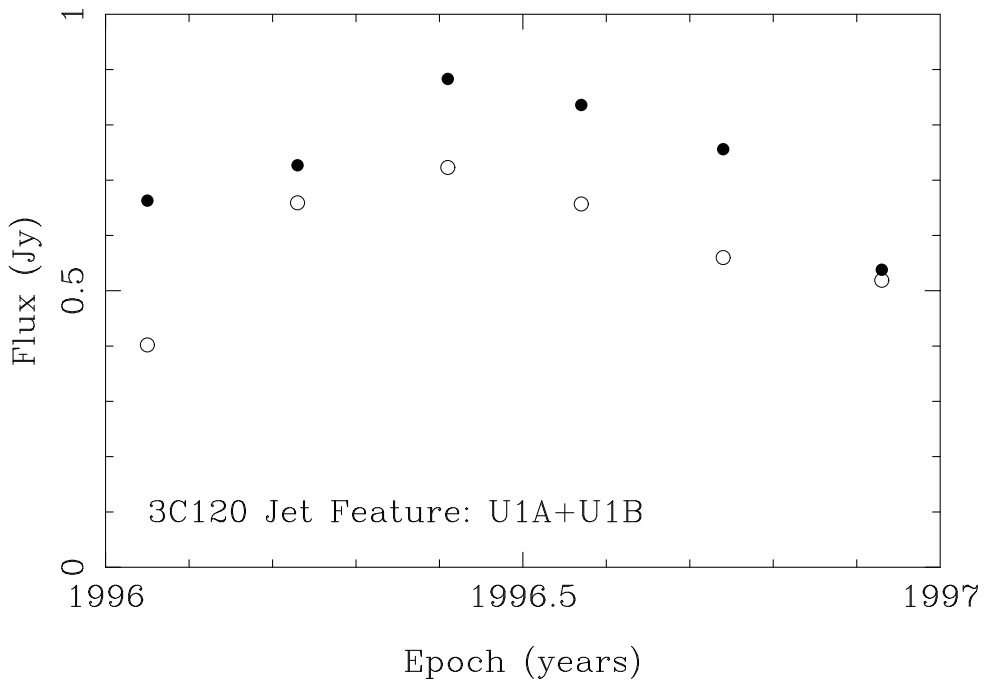


FIG. 16.—Flux of the jet feature, U1A+U1B (K1A+K1B) in 3C 120, plotted against epoch. Filled and open circles represent measurements at 15 and 22 GHz, respectively.

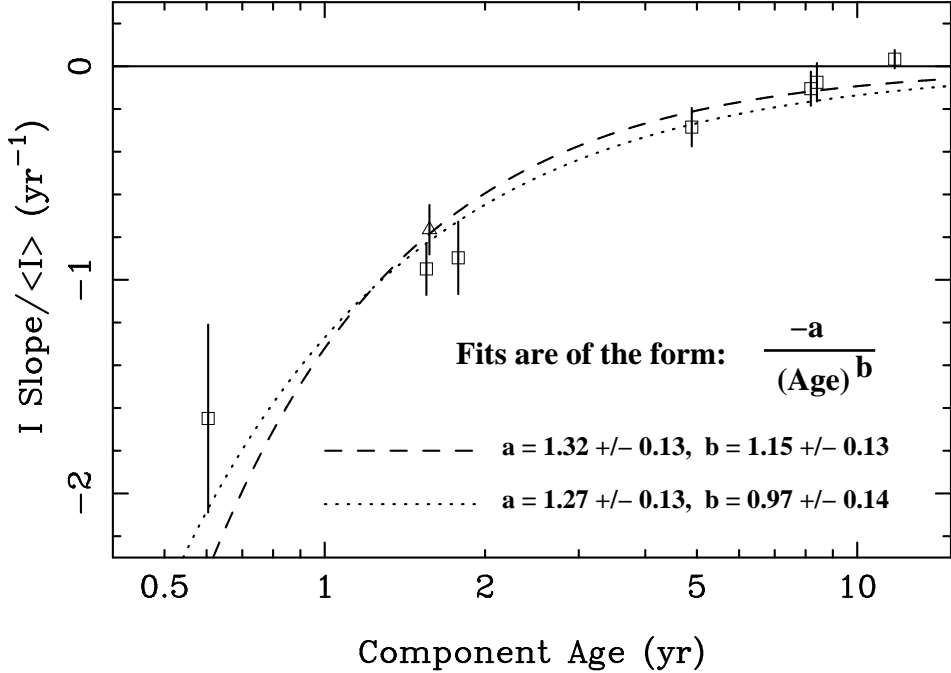


FIG. 17.— Fractional flux slope, $\langle \dot{I}/\langle I \rangle \rangle$, for jet features plotted against the apparent age of the feature in our frame. Fits to the model, $(dI/dt)/\langle I \rangle = -a/T_{\text{age}}^b$, are plotted and discussed in the text, §4.1.1. The open triangle represents the jet feature U1A+U1B (K1A+K1B) from 3C 120 for only the last four epochs when its flux decayed (see the text).

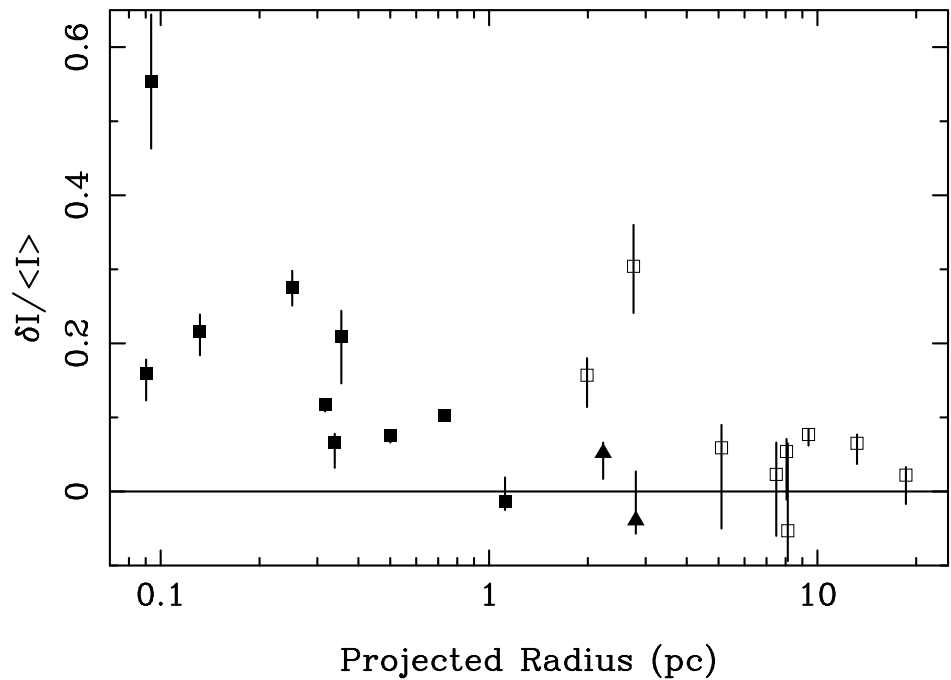


FIG. 18.— Standard deviation of the correlated fluctuations in flux divided by the mean flux, $\delta I/\langle I \rangle$, plotted against projected radius in parsecs. Filled squares represent core regions, and open squares represent jet features. J0738+17 and J1312+32, where we have analyzed the total VLBI flux of the source, are represented by filled triangles.

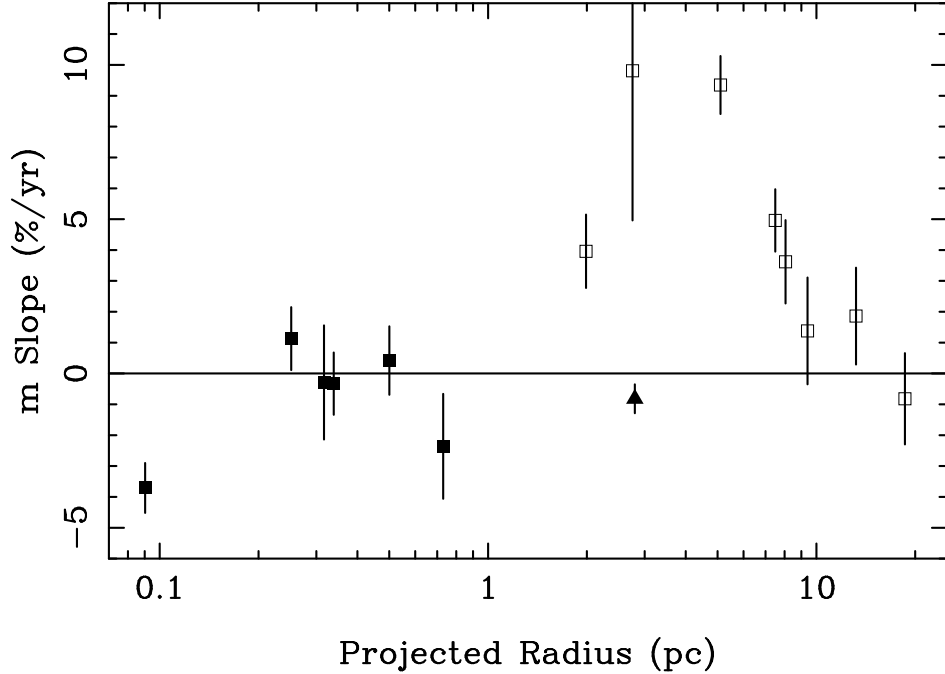


FIG. 19.— Fractional polarization slope, $\langle m \rangle$ (see table 5), plotted against projected radius in parsecs. Filled squares represent core regions, and open squares represent jet features. J1312+32, where we have analyzed the total VLBI flux of the source, is represented by a filled triangle.

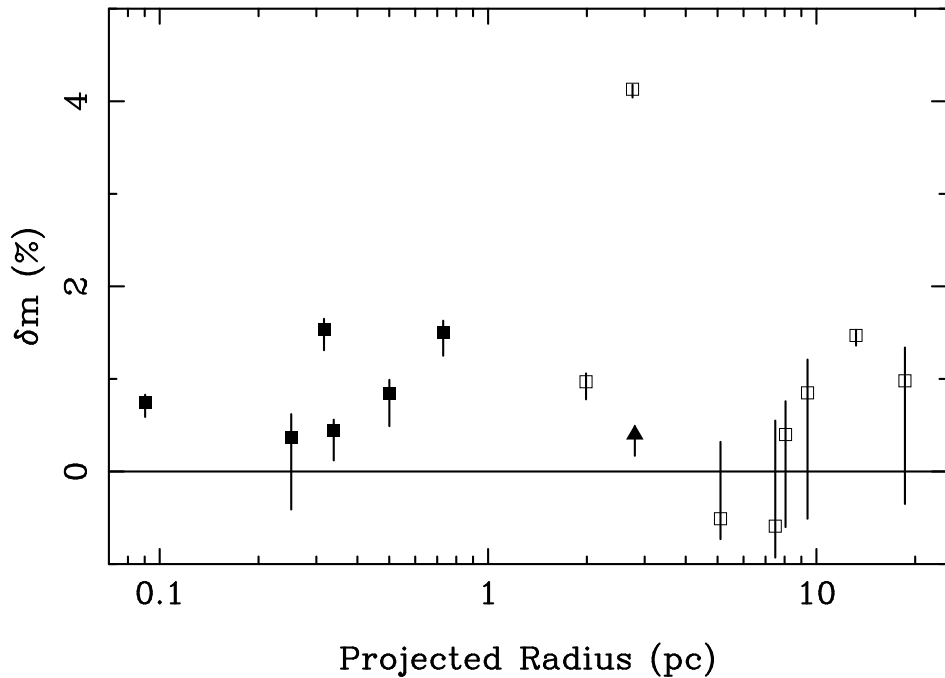


FIG. 20.— Standard deviation of the correlated fractional polarization fluctuations, δm , plotted against projected radius in parsecs. Filled squares represent core regions, and open squares represent jet features. J1312+32, where we have analyzed the total VLBI flux of the source, is represented by a filled triangle. The high point in the figure at 4% is the jet feature, U3, from OJ287.

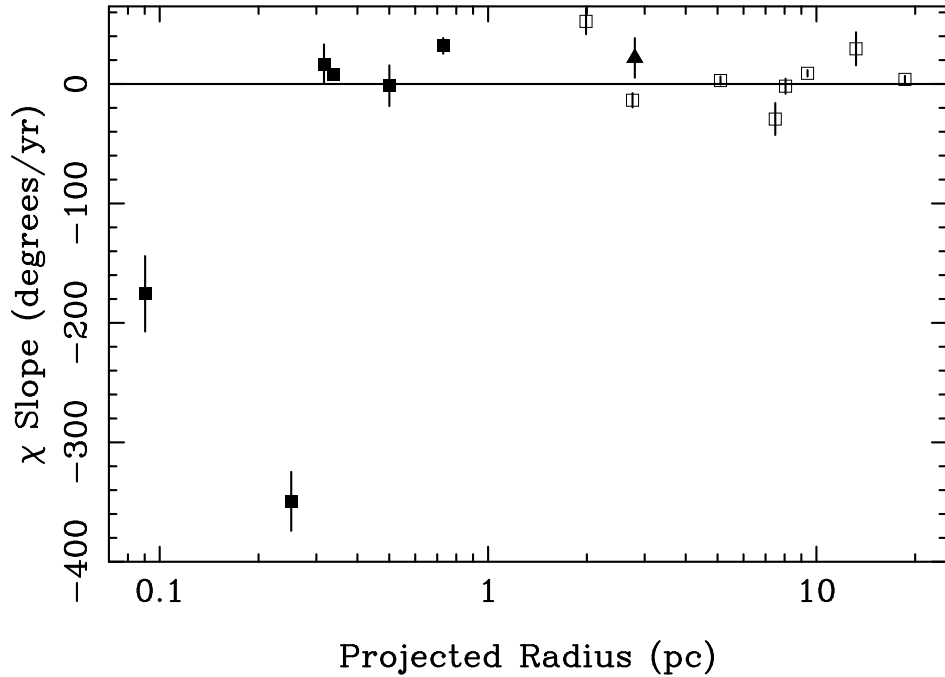


FIG. 21.—Polarization angle slope, $\langle \dot{\chi} \rangle$ (see table 6), plotted against projected radius in parsecs. Filled squares represent core regions, and open squares represent jet features. J1312+32, where we have analyzed the total VLBI flux of the source, is represented by a filled triangle.

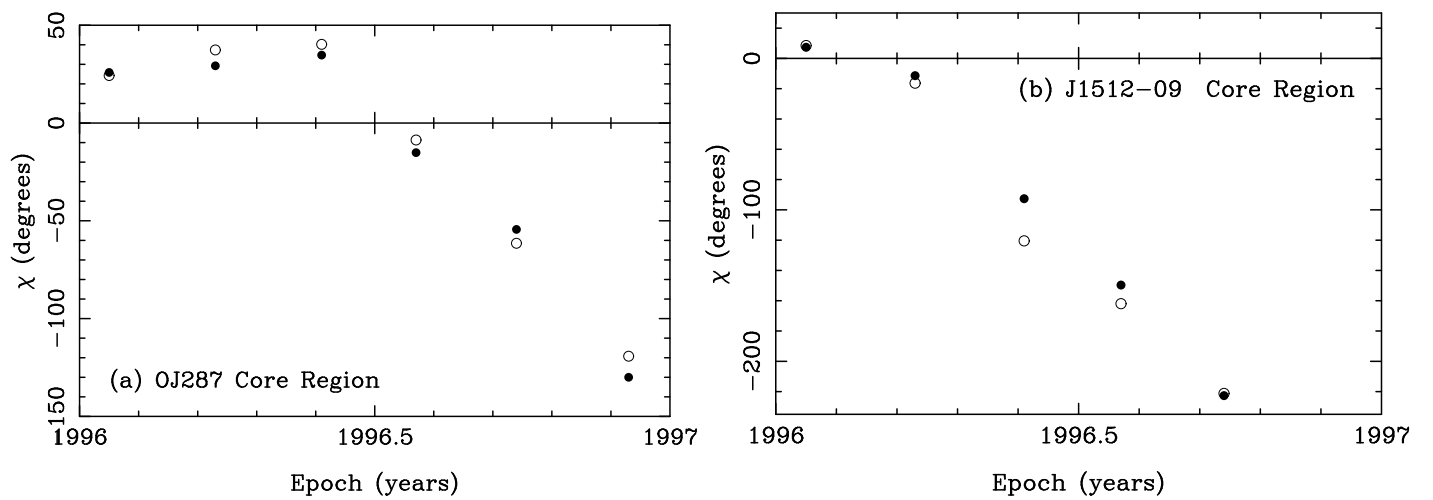


FIG. 22.—Polarization angle, χ , plotted against epoch for the core regions of OJ287 (panel (a)) and J1512-09 (panel (b)). Filled and open circles represent measurements at 15 and 22 GHz, respectively.

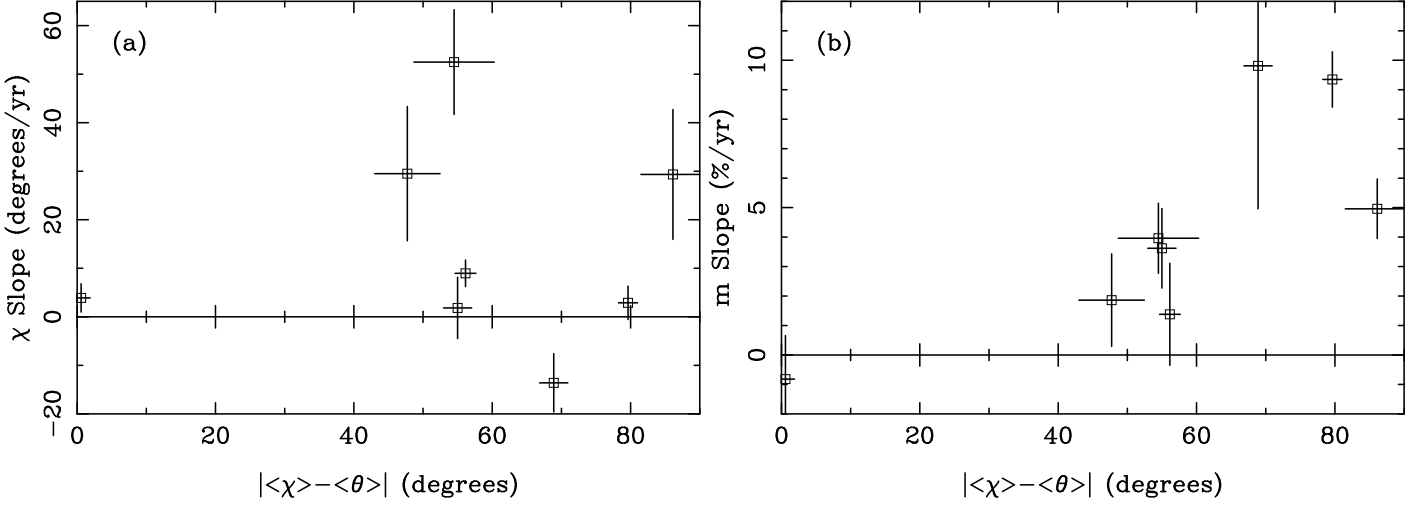


FIG. 23.— Plots of polarization angle slope, $\langle\dot{\chi}\rangle$, (panel (a)) and fractional polarization slope, $\langle\dot{m}\rangle$, (panel (b)) versus the “mis-alignment” between mean polarization angle, $\langle\chi\rangle$, and mean structural position angle, $\langle\theta\rangle$, of jet features. $|\langle\chi\rangle - \langle\theta\rangle| = 90^\circ$ indicates magnetic field aligned parallel to the structural position angle. In panel (a), the polarization angle slopes are positive if they are rotations in the direction of aligning the magnetic field with the structural position angle.

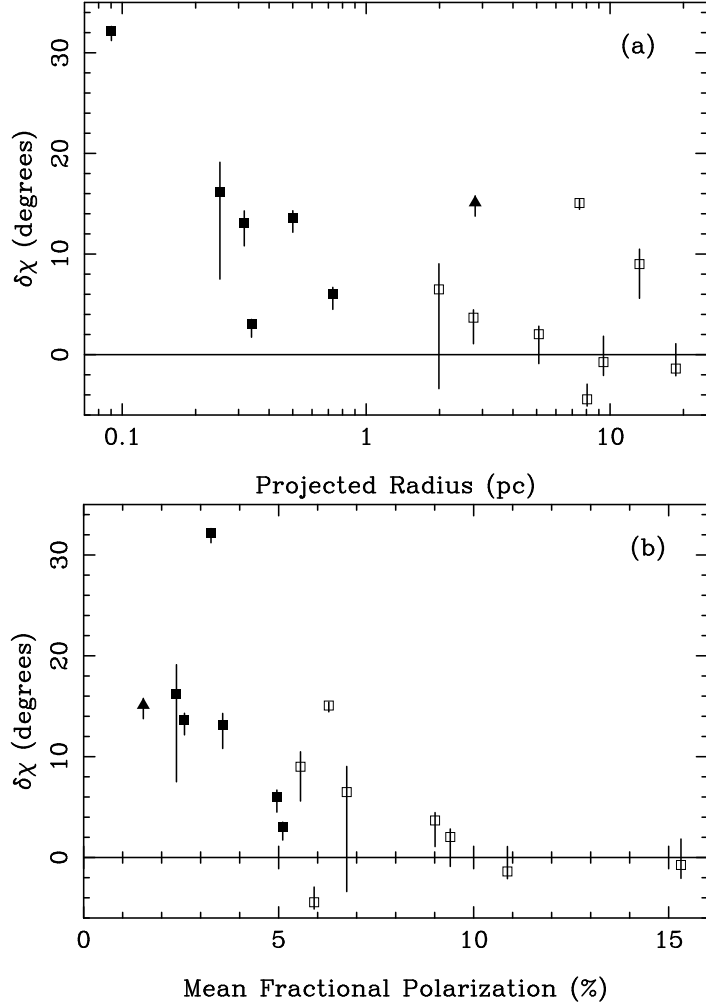


FIG. 24.— Standard deviation of the correlated polarization angle fluctuations, $\delta\chi$, plotted against projected radius in parsecs in panel (a). In panel (b), the standard deviation is plotted against mean fractional polarization. Filled squares represent core regions, and open squares represent jet features. J1312+32, where we have analyzed the total VLBI flux of the source, is represented by a filled triangle.

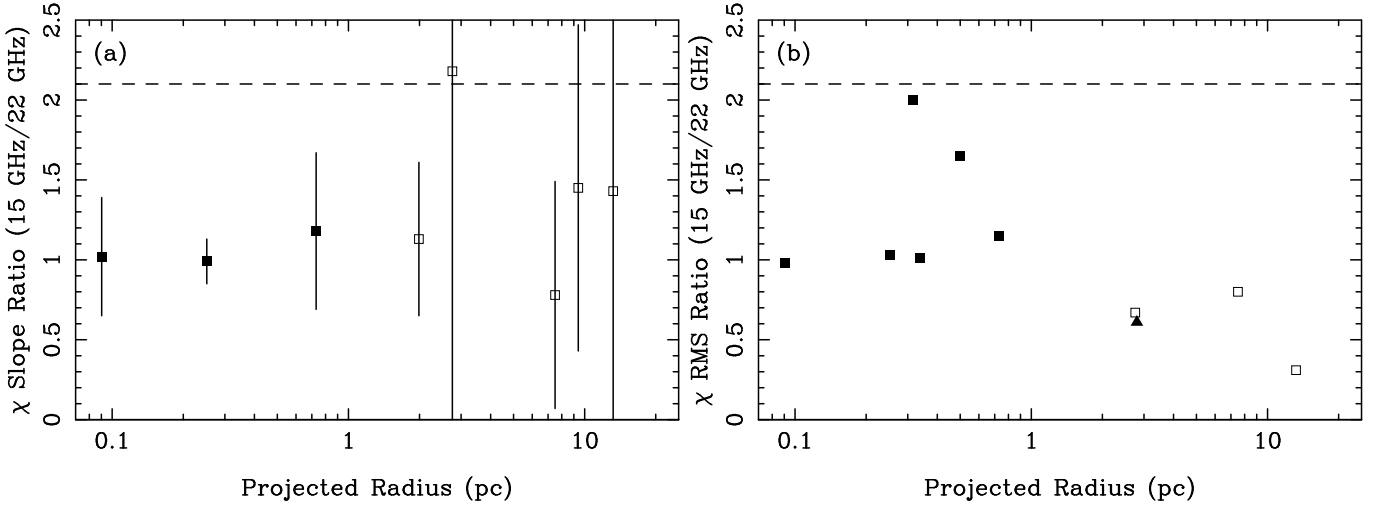


FIG. 25.—Ratio of χ changes at 15 GHz to those at 22 GHz plotted against projected radius. Panel (a) displays the ratio of linear χ slopes at the two frequencies. Only features with a mean χ slope greater than 2σ are plotted. Panel (b) displays the ratio of the RMS fluctuations at the two frequencies. Only features where the fluctuations are correlated at the $r > 0.5$ level are plotted. Filled squares represent core regions, and open squares represent jet features. J1312+32, where we have analyzed the total VLBI flux of the source, is represented by a filled triangle. The dashed lines indicate where the points should cluster if Faraday rotation was primarily responsible for the observed polarization angle changes.

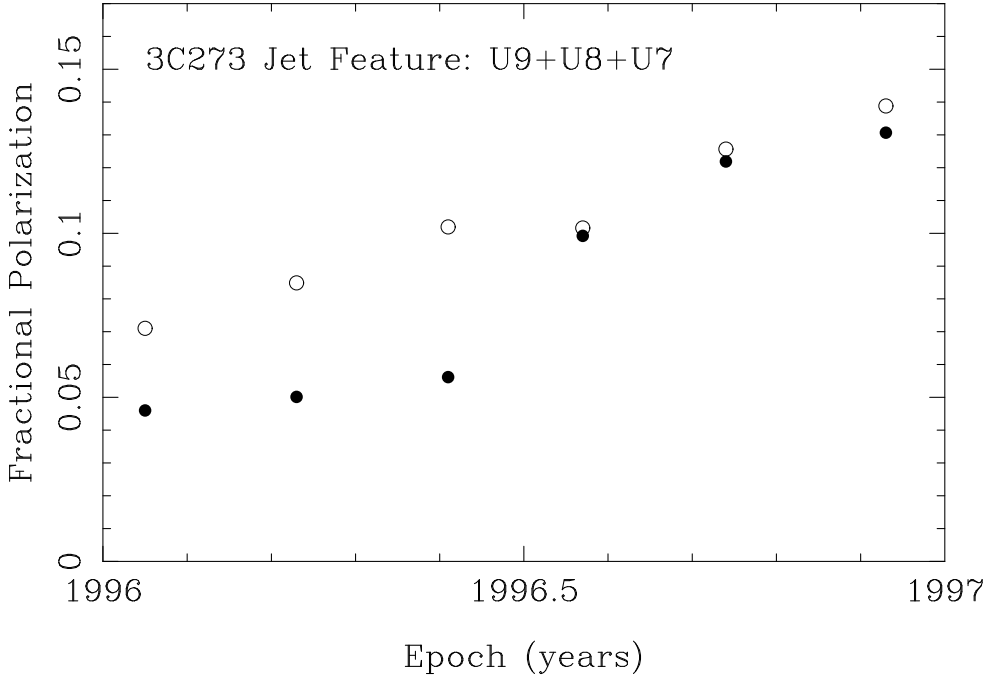


FIG. 26.—Fractional polarization of the jet feature, U9+U8+U7 (K9+K8+K7) in 3C 273, plotted against epoch. Filled and open circles represent measurements at 15 and 22 GHz, respectively.

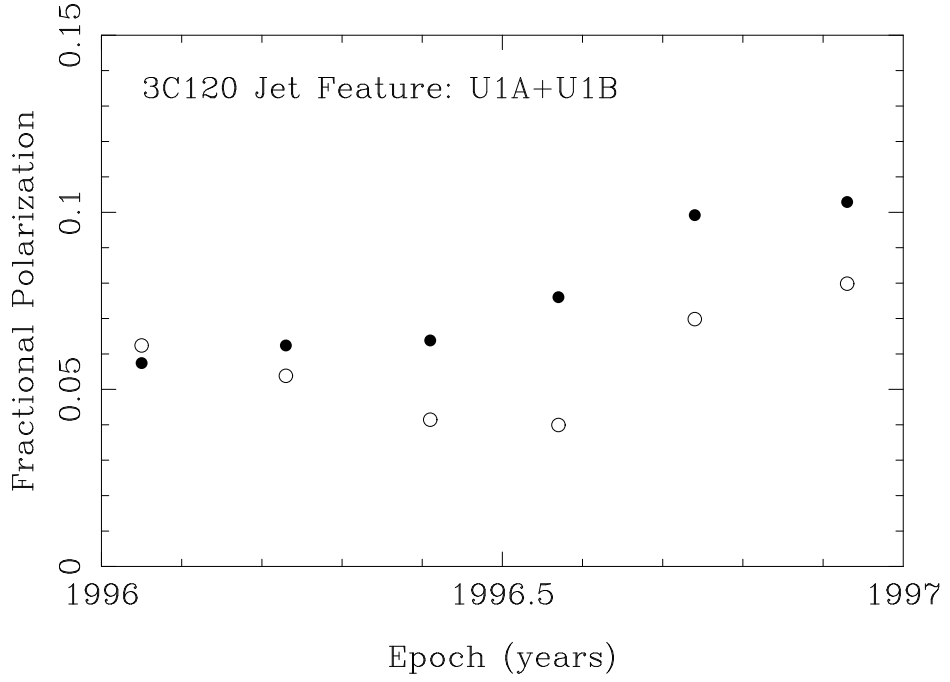


FIG. 27.— Fractional polarization of the jet feature, U1A+U1B (K1A+K1B) in 3C 120, plotted against epoch. Filled and open circles represent measurements at 15 and 22 GHz, respectively.

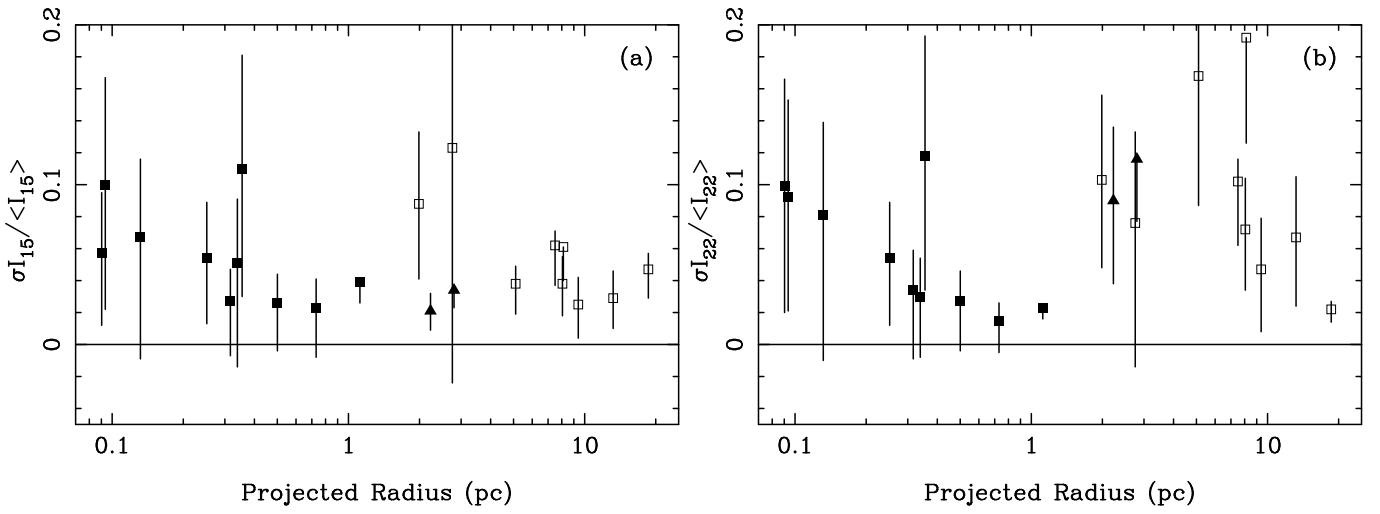


FIG. 28.— Fractional flux uncertainty estimates at 15 GHz (panel (a)) and 22 GHz (panel (b)) plotted against projected radius. Filled squares represent core regions, and open squares represent jet features. J0738+17 and J1312+32, where we have analyzed the total VLBI flux of the source, are represented by filled triangles.

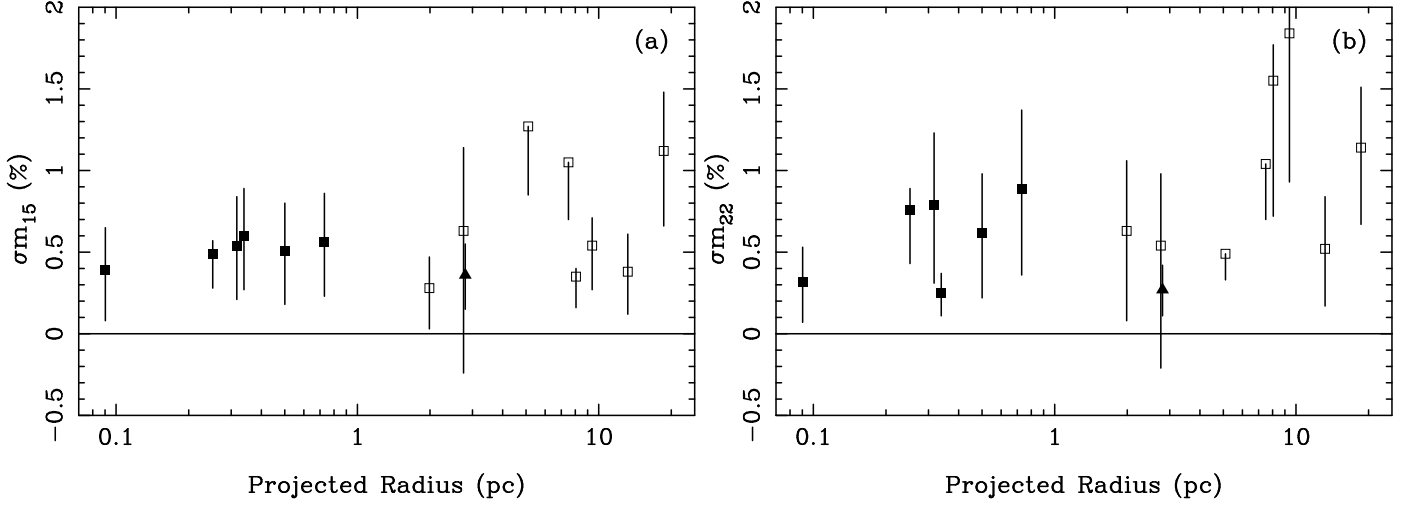


FIG. 29.— Fractional polarization uncertainty estimates at 15 GHz (panel (a)) and 22 GHz (panel (b)) plotted against projected radius. Filled squares represent core regions, and open squares represent jet features. J1312+32, where we have analyzed the total VLBI flux of the source, is represented by a filled triangle.

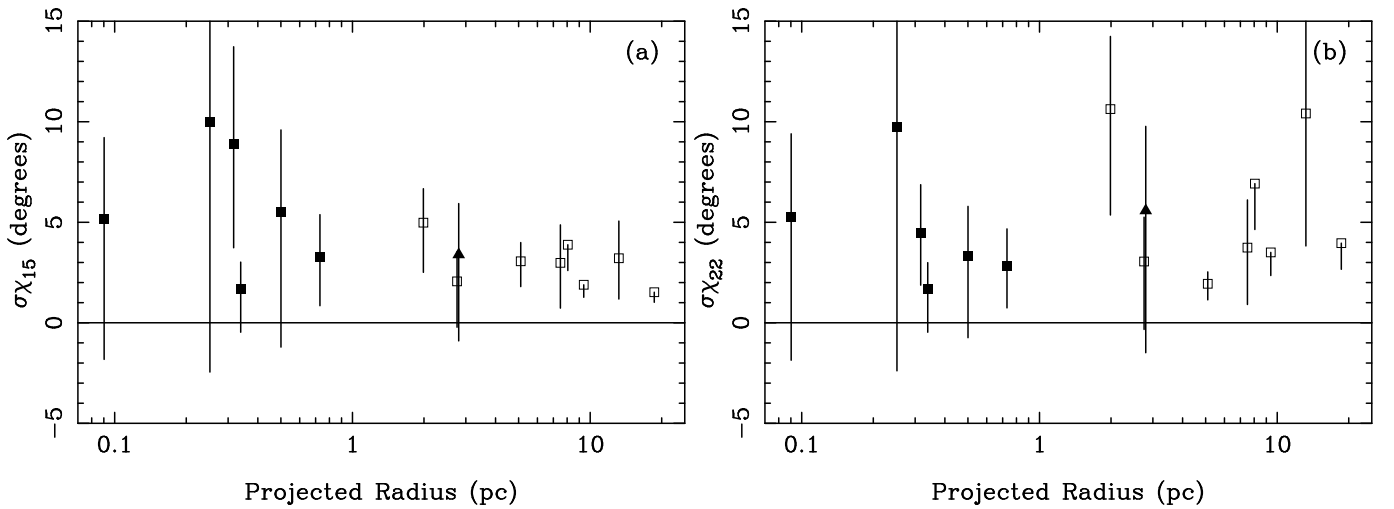


FIG. 30.— Polarization angle uncertainty estimates at 15 GHz (panel (a)) and 22 GHz (panel (b)) plotted against projected radius. Filled squares represent core regions, and open squares represent jet features. J1312+32, where we have analyzed the total VLBI flux of the source, is represented by a filled triangle.

TABLE 1
SOURCE INFORMATION

J2000.0	J1950.0	Other Names	Redshift	Classification
J0433+053	B0430+052	3C 120, II Zw 14	0.033	Sy 1
J0530+135	B0528+134	PKS 0528+134	2.060	Quasar
J0738+177	B0735+178	OI 158, DA 237, PKS 0735+178	0.424 ^a	BL
J0854+201	B0851+202	OJ 287	0.306	BL
J1224+212	B1222+216	4C 21.35	0.435	Quasar
J1229+020	B1226+023	3C 273	0.158	Quasar
J1256-057	B1253-055	3C 279	0.536	Quasar
J1310+323	B1308+326	OP 313	0.996	Quasar/BL
J1512-090	B1510-089	OR -017	0.360	Quasar
J1751+09	B1749+096	OT 081, 4C 09.56	0.322	BL
J1927+739	B1928+738	4C 73.18	0.302	Quasar
J2005+778	B2007+777		0.342	BL

^aLower limit

TABLE 2
JET FEATURES.

Object	Jet Feature	$\langle R \rangle$ (pc)	$\langle \theta \rangle$ (deg.)	N_I	N_P
3C 120	KD+K3+K2/UD+U2 K1A+K1B/U1A+U1B	0.13 1.99	-121.5 -110.3	6 6	...
J0530+13	KD+K2/UD+U2	0.50	91.3	6	5
J0738+17	KALL/UALL	2.23	65.4	6	...
OJ287	KD+K4/UD+U4 K3/U3	0.09 2.76	-106.1 -94.7	6 6	5
J1224+21	KD+K4+K3/UD+U3	0.34	-14.2	5	5
3C 273	KD+K10/UD+U10 K9+K8+K7/U9+U8+U7 K4+K5/U4+U5	0.35 5.11 13.2	-118.2 -118.2 -111.4	6 6 6	...
3C 279	KD+K4/UD+U4 K1+K2/U1+U2	0.32 18.6	-119.0 -114.6	6 6	6
J1310+32	KALL/UALL	2.80	-63.1	6	5
J1512-09	KD+K2/UD+U2 K1/U1	0.25 7.49	-32.7 -28.6	6 6	5
J1751+09	KD/UD+U3	0.09	35.1	6	...
J1927+73	KD+K3/UD+U3 K2/U2 K1/U1	1.12 8.06 9.41	150.8 157.3 172.9	6 6 6	...
J2005+77	KD+K2/UD+U3+U2 K1/U1	0.73 8.13	-91.0 -94.1	6 6	...

Note. — The mean radial position of the jet feature is given by $\langle R \rangle$ at a mean structural position angle of $\langle \theta \rangle$ (measured counter clockwise from north). N_I is the number of epochs available for total intensity variability analysis, and N_P is the number of epochs available for polarization variability analysis. Not all features have adequate polarization strength in at least five epochs (at both frequencies) to be used for variability analysis; these cases are indicated by See §2.4 for a description of our selection criteria.

TABLE 3
MEAN PROPERTIES OF JET FEATURES.

Object	Jet Feature	$\langle I_{15} \rangle$ (Jy)	$\langle I_{22} \rangle$ (Jy)	$\langle m_{15} \rangle$ (%)	$\langle m_{22} \rangle$ (%)	$\langle \chi_{15} \rangle$ (deg.)	$\langle \chi_{22} \rangle$ (deg.)
3C 120	KD+K3+K2/UD+U2	1.54 ± 0.19	1.75 ± 0.22
	K1A+K1B/U1A+U1B	0.73 ± 0.05	0.59 ± 0.05	7.7 ± 0.8	5.8 ± 0.6	-59.2 ± 7.8	-52.4 ± 8.4
J0530+13	KD+K2/UD+U2	8.01 ± 0.40	7.90 ± 0.51	2.0 ± 0.4	3.1 ± 0.5	-98.6 ± 8.2	-104.9 ± 5.0
J0738+17	KALL/UALL	0.97 ± 0.07	0.89 ± 0.07
OJ287	KD+K4/UD+U4	1.15 ± 0.09	1.29 ± 0.11	3.2 ± 0.6	3.3 ± 0.5	-18.3 ± 26.3	-14.6 ± 26.1
	K3/U3	0.48 ± 0.13	0.41 ± 0.10	9.7 ± 2.0	8.3 ± 1.7	-26.6 ± 2.7	-25.1 ± 2.3
J1224+21	KD+K4+K3/UD+U3	1.47 ± 0.08	1.49 ± 0.08	5.5 ± 0.4	4.7 ± 0.2	-38.8 ± 1.4	-36.6 ± 2.1
3C 273	KD+K10/UD+U10	10.38 ± 1.81	14.22 ± 1.79
	K9+K8+K7/U9+U8+U7	5.24 ± 0.73	4.16 ± 0.53	8.4 ± 1.6	10.4 ± 1.0	-35.7 ± 1.6	-41.4 ± 1.0
	K4+K5/U4+U5	1.41 ± 0.06	1.32 ± 0.08	6.2 ± 0.5	4.9 ± 0.7	123.2 ± 5.1	109.4 ± 7.7
3C 279	KD+K4/UD+U4	15.03 ± 0.85	19.35 ± 0.96	2.7 ± 0.6	4.4 ± 0.8	50.0 ± 8.4	48.2 ± 4.2
	K1+K2/U1+U2	2.48 ± 0.06	2.19 ± 0.02	10.6 ± 0.6	11.1 ± 0.6	65.2 ± 0.6	66.8 ± 1.6
J1310+32	KALL/UALL	2.79 ± 0.13	2.48 ± 0.13	1.8 ± 0.3	1.3 ± 0.2	26.7 ± 5.5	27.3 ± 9.0
J1512-09	KD+K2/UD+U2	1.19 ± 0.14	1.42 ± 0.16	1.9 ± 0.3	2.8 ± 0.4	-93.8 ± 42.9	-102.3 ± 43.4
	K1/U1	0.43 ± 0.06	0.31 ± 0.04	6.0 ± 0.7	6.6 ± 0.8	67.3 ± 5.6	63.2 ± 7.1
J1751+09	KD/UD+U3	1.34 ± 0.32	1.50 ± 0.33
J1927+73	KD+K3/UD+U3	2.28 ± 0.06	2.37 ± 0.03
	K2/U2	0.39 ± 0.01	0.31 ± 0.01	5.4 ± 0.6	6.4 ± 0.9	-75.7 ± 1.7	-79.7 ± 3.1
	K1/U1	0.39 ± 0.02	0.29 ± 0.01	15.2 ± 0.4	15.5 ± 0.9	48.1 ± 1.6	49.9 ± 1.6
J2005+77	KD+K2/UD+U3+U2	0.82 ± 0.04	0.88 ± 0.04	5.2 ± 0.5	4.7 ± 0.9	83.3 ± 5.3	83.1 ± 4.5
	K1/U1	0.11 ± 0.01	0.07 ± 0.01

Note. — Total intensity is denoted by I , fractional linear polarization by m , and polarization position angle by χ (measured counterclockwise from north). Mean values are averages across all epochs used for variability analysis. Subscripts denote the frequency of observation in GHz.

TABLE 4
FLUX VARIABILITY.

Object	Jet Feature	Linear Slopes with Time			Correlated Fluctuations		
		$\dot{I}_{15}/\langle I_{15} \rangle$ (yr $^{-1}$)	$\dot{I}_{22}/\langle I_{22} \rangle$ (yr $^{-1}$)	$\langle \dot{I}/\langle I \rangle \rangle$ (yr $^{-1}$)	r	p_r	$\delta I/\langle I \rangle$
3C 120	KD+K3+K2/UD+U2	0.74 ± 0.30	0.63 ± 0.35	0.69 ± 0.23	0.90	0.02	0.22 (+0.02, -0.03)
	K1A+K1B/U1A+U1B	-0.13 ± 0.25	0.07 ± 0.30	-0.03 ± 0.20	0.73	0.05	0.16 (+0.02, -0.04)
J0530+13	KD+K2/UD+U2	-0.31 ± 0.11	-0.43 ± 0.12	-0.37 ± 0.08	0.89	0.02	0.08 (+0.01, -0.01)
J0738+17	KALL/UALL	-0.56 ± 0.06	-0.47 ± 0.20	-0.51 ± 0.10	0.58	0.15	0.05 (+0.01, -0.04)
OJ287	KD+K4/UD+U4	0.42 ± 0.19	0.18 ± 0.32	0.30 ± 0.18	0.82	0.05	0.16 (+0.02, -0.04)
	K3/U3	-1.65 ± 0.71	-1.65 ± 0.52	-1.65 ± 0.44	0.91	0.02	0.30 (+0.06, -0.06)
J1224+21	KD+K4+K3/UD+U3	-0.28 ± 0.18	-0.40 ± 0.11	-0.34 ± 0.11	0.74	0.13	0.07 (+0.01, -0.03)
3C 273	KD+K10/UD+U10	1.14 ± 0.37	0.66 ± 0.35	0.90 ± 0.26	0.77	0.06	0.21 (+0.03, -0.06)
	K9+K8+K7/U9+U8+U7	-1.03 ± 0.16	-0.76 ± 0.30	-0.90 ± 0.17	0.35	0.28	0.06 (+0.03, -0.11)
	K4+K5/U4+U5	-0.29 ± 0.07	-0.28 ± 0.17	-0.29 ± 0.09	0.69	0.10	0.07 (+0.01, -0.03)
3C 279	KD+K4/UD+U4	0.30 ± 0.15	0.04 ± 0.19	0.17 ± 0.12	0.94	0.01	0.12 (+0.01, -0.01)
	K1+K2/U1+U2	0.09 ± 0.08	-0.02 ± 0.04	0.03 ± 0.04	0.33	0.26	0.02 (+0.01, -0.04)
J1310+32	KALL/UALL	-0.33 ± 0.05	-0.25 ± 0.16	-0.29 ± 0.08	-0.40	0.26	-0.04 (+0.07, -0.02)
J1512-09	KD+K2/UD+U2	-0.27 ± 0.41	-0.31 ± 0.40	-0.29 ± 0.29	0.96	0.00	0.27 (+0.02, -0.02)
	K1/U1	-0.97 ± 0.15	-0.93 ± 0.19	-0.95 ± 0.12	0.08	0.45	0.02 (+0.04, -0.08)
J1751+09	KD/UD+U3	-0.61 ± 0.86	-0.18 ± 0.82	-0.39 ± 0.60	0.97	0.00	0.55 (+0.09, -0.09)
J1927+73	KD+K3/UD+U3	0.18 ± 0.05	0.06 ± 0.03	0.12 ± 0.03	-0.20	0.37	-0.01 (+0.03, -0.01)
	K2/U2	-0.25 ± 0.08	0.04 ± 0.14	-0.10 ± 0.08	0.52	0.18	0.05 (+0.02, -0.07)
	K1/U1	-0.30 ± 0.08	0.15 ± 0.16	-0.08 ± 0.09	0.83	0.04	0.08 (+0.01, -0.02)
J2005+77	KD+K2/UD+U3+U2	-0.03 ± 0.18	0.25 ± 0.11	0.11 ± 0.11	0.97	0.00	0.10 (+0.00, -0.00)
	K1/U1	-0.61 ± 0.10	-0.55 ± 0.27	-0.58 ± 0.14	-0.24	0.35	-0.05 (+0.12, -0.04)

Note. — $\dot{I}_{15}/\langle I_{15} \rangle$ and $\dot{I}_{22}/\langle I_{22} \rangle$ are the fractional flux slopes with time for 15 and 22 GHz respectively. $\langle \dot{I}/\langle I \rangle \rangle$ is the mean of these slopes. §3 describes our analysis for fluctuations that correlate between 15 and 22 GHz: r is the correlation coefficient, and p_r is the probability of obtaining a correlation this strong by pure chance. $\delta I/\langle I \rangle$ is the standard deviation of the correlated fluctuations divided by the mean flux (across epoch and frequency).

TABLE 5
FRACTIONAL POLARIZATION VARIABILITY.

Object	Jet Feature	Linear Slopes with Time			Correlated Fluctuations		
		\dot{m}_{15} (%/yr)	\dot{m}_{22} (%/yr)	$\langle \dot{m} \rangle$ (%/yr)	r	p_r	δm (%)
3C 120	K1A+K1B/U1A+U1B	5.7 ± 1.0	2.2 ± 2.2	4.0 ± 1.2	0.84	0.04	1.0 (+0.1, -0.2)
J0530+13	KD+K2/UD+U2	1.1 ± 1.3	-0.2 ± 1.8	0.4 ± 1.1	0.69	0.10	0.8 (+0.2, -0.3)
OJ287	KD+K4/UD+U4 K3/U3	-4.1 ± 1.3 9.6 ± 7.7	-3.4 ± 1.0 10.0 ± 5.8	-3.7 ± 0.8 9.8 ± 4.8	0.82 0.98	0.05 0.00	0.7 (+0.1, -0.2) 4.1 (+0.0, -0.1)
J1224+21	KD+K4+K3/UD+U3	-0.8 ± 1.9	0.1 ± 0.8	-0.3 ± 1.0	0.56	0.16	0.4 (+0.1, -0.3)
3C 273	K9+K8+K7/U9+U8+U7 K4+K5/U4+U5	11.1 ± 1.8 2.0 ± 1.8	7.6 ± 0.7 1.7 ± 2.6	9.4 ± 0.9 1.9 ± 1.6	-0.41 0.92	0.25 0.01	-0.5 (+0.8, -0.2) 1.5 (+0.1, -0.1)
3C 279	KD+K4/UD+U4 K1+K2/U1+U2	0.4 ± 2.1 -2.5 ± 1.9	-1.0 ± 3.0 0.9 ± 2.3	-0.3 ± 1.9 -0.8 ± 1.5	0.84 0.43	0.02 0.20	1.5 (+0.1, -0.2) 1.0 (+0.4, -1.3)
J1310+32	KALL/UALL	-1.0 ± 0.7	-0.7 ± 0.6	-0.8 ± 0.5	0.62	0.13	0.4 (+0.1, -0.2)
J1512-09	KD+K2/UD+U2 K1/U1	1.2 ± 1.0 4.3 ± 1.4	1.0 ± 1.8 5.6 ± 1.4	1.1 ± 1.0 5.0 ± 1.0	0.27 -0.32	0.33 0.30	0.4 (+0.3, -0.8) -0.6 (+1.1, -0.3)
J1927+73	K2/U2 K1/U1	3.9 ± 0.6 2.8 ± 1.0	3.4 ± 2.6 -0.0 ± 3.3	3.6 ± 1.4 1.4 ± 1.7	0.23 0.42	0.39 0.24	0.4 (+0.4, -1.0) 0.8 (+0.4, -1.4)
J2005+77	KD+K2/UD+U3+U2	-2.6 ± 1.5	-2.1 ± 3.0	-2.4 ± 1.7	0.82	0.02	1.5 (+0.1, -0.2)

Note. — \dot{m}_{15} and \dot{m}_{22} are the fractional polarization slopes with time for 15 and 22 GHz respectively. $\langle \dot{m} \rangle$ is the mean of these slopes. §3 describes our analysis for fluctuations that correlate between 15 and 22 GHz: r is the correlation coefficient, and p_r is the probability of obtaining a correlation this strong by pure chance. δm is the standard deviation of the correlated fluctuations.

TABLE 6
POLARIZATION ANGLE VARIABILITY.

Object	Jet Feature	Linear Slopes with Time			Correlated Fluctuations		
		$\dot{\chi}_{15}$ (deg./yr)	$\dot{\chi}_{22}$ (deg./yr)	$\langle \dot{\chi} \rangle$ (deg./yr)	r	p_r	$\delta\chi$ (deg.)
3C 120	K1A+K1B/U1A+U1B	55.6 ± 9.2	49.4 ± 19.6	52.5 ± 10.8	0.44	0.23	$6.5 (+2.5, -9.9)$
J0530+13	KD+K2/UD+U2	1.0 ± 29.3	-3.8 ± 17.6	-1.4 ± 17.1	0.91	0.02	$13.6 (+0.7, -1.4)$
OJ287	KD+K4/UD+U4 K3/U3	-177.3 ± 44.3 -18.6 ± 6.7	-174.1 ± 45.2 -8.6 ± 9.9	-175.7 ± 31.6 -13.6 ± 6.0	0.97 0.68	0.00 0.16	$32.1 (+0.5, -0.9)$ $3.7 (+0.8, -2.6)$
J1224+21	KD+K4+K3/UD+U3	2.8 ± 6.4	13.1 ± 6.3	8.0 ± 4.5	0.77	0.12	$3.0 (+0.5, -1.3)$
3C 273	K9+K8+K7/U9+U8+U7 K4+K5/U4+U5	4.2 ± 5.7 34.7 ± 8.2	1.5 ± 3.8 24.3 ± 26.5	2.9 ± 3.4 29.5 ± 13.8	0.41 0.71	0.21 0.09	$2.0 (+0.8, -2.9)$ $9.0 (+1.5, -3.4)$
3C 279	KD+K4/UD+U4 K1+K2/U1+U2	15.2 ± 30.6 2.7 ± 1.9	17.9 ± 13.0 5.1 ± 5.5	16.5 ± 16.6 3.9 ± 2.9	0.81 -0.32	0.02 0.27	$13.1 (+1.2, -2.3)$ $-1.4 (+2.5, -0.7)$
J1310+32	KALL/UALL	22.9 ± 14.4	20.8 ± 29.9	21.8 ± 16.6	0.92	0.01	$15.1 (+0.7, -1.4)$
J1512-09	KD+K2/UD+U2 K1/U1	-347.0 ± 35.3 -25.7 ± 16.8	-351.9 ± 34.4 -33.0 ± 20.8	-349.4 ± 24.7 -29.3 ± 13.4	0.73 0.95	0.14 0.00	$16.2 (+2.9, -8.7)$ $15.1 (+0.3, -0.6)$
J1927+73	K2/U2 K1/U1	-7.8 ± 4.9 10.6 ± 2.6	4.1 ± 11.7 7.3 ± 4.8	-1.8 ± 6.3 9.0 ± 2.7	-0.73 -0.08	0.08 0.45	$-4.4 (+1.5, -0.7)$ $-0.7 (+2.6, -1.3)$
J2005+77	KD+K2/UD+U3+U2	34.6 ± 9.9	29.2 ± 8.6	31.9 ± 6.6	0.80	0.05	$6.0 (+0.7, -1.5)$

Note. — $\dot{\chi}_{15}$ and $\dot{\chi}_{22}$ are the polarization position angle slopes with time for 15 and 22 GHz respectively. $\langle \dot{\chi} \rangle$ is the mean of these slopes. §3 describes our analysis for fluctuations that correlate between 15 and 22 GHz: r is the correlation coefficient, and p_r is the probability of obtaining a correlation this strong by pure chance. $\delta\chi$ is the standard deviation of the correlated fluctuations.

TABLE 7
SPECTRAL PROPERTIES.

Object	Jet Feature	$\langle \alpha \rangle$	$\dot{\alpha}$ (yr $^{-1}$)	$\langle m_{ratio} \rangle$	\dot{m}_{ratio} (yr $^{-1}$)	$\langle \Delta \chi \rangle$ (deg.)	$\dot{\Delta \chi}$ (deg./yr)
3C 120	KD+K3+K2/UD+U2 K1A+K1B/U1A+U1B	0.35 ± 0.12 -0.62 ± 0.18	-0.29 ± 0.41 0.76 ± 0.56	\dots 1.37 ± 0.14	\dots 0.49 ± 0.46	\dots -6.8 ± 4.7	\dots 6.2 ± 17.5
J0530+13	KD+K2/UD+U2	-0.05 ± 0.06	-0.35 ± 0.14	0.67 ± 0.14	0.42 ± 0.43	6.4 ± 4.2	4.8 ± 14.9
J0738+17	KALL/UALL	-0.23 ± 0.13	0.28 ± 0.45	\dots	\dots	\dots	\dots
OJ287	KD+K4/UD+U4 K3/U3	0.31 ± 0.17 -0.37 ± 0.20	-0.56 ± 0.57 -0.46 ± 0.72	0.95 ± 0.06 1.19 ± 0.06	-0.17 ± 0.21 -0.28 ± 0.23	-3.7 ± 2.7 -1.5 ± 2.0	-3.2 ± 10.2 -10.1 ± 7.3
J1224+21	KD+K4+K3/UD+U3	0.03 ± 0.08	-0.33 ± 0.33	1.19 ± 0.08	-0.24 ± 0.33	-2.2 ± 1.6	-10.3 ± 4.3
3C 273	KD+K10/UD+U10 K9+K8+K7/U9+U8+U7 K4+K5/U4+U5	1.01 ± 0.27 -0.58 ± 0.26 -0.18 ± 0.09	-1.75 ± 0.54 1.06 ± 0.81 0.02 ± 0.33	\dots 0.78 ± 0.08 1.33 ± 0.11	\dots 0.49 ± 0.19 0.14 ± 0.41	\dots 5.8 ± 1.5 13.8 ± 5.9	\dots 2.7 ± 5.6 10.4 ± 21.5
3C 279	KD+K4/UD+U4 K1+K2/U1+U2	0.69 ± 0.11 -0.33 ± 0.06	-0.75 ± 0.15 -0.29 ± 0.17	0.62 ± 0.07 0.96 ± 0.05	0.29 ± 0.24 -0.29 ± 0.15	1.8 ± 5.5 -1.6 ± 1.9	-2.7 ± 20.8 -2.3 ± 7.1
J1310+32	KALL/UALL	-0.32 ± 0.14	0.29 ± 0.49	1.43 ± 0.19	-0.08 ± 0.69	-0.7 ± 4.5	2.1 ± 16.0
J1512-09	KD+K2/UD+U2 K1/U1	0.48 ± 0.09 -0.93 ± 0.13	0.01 ± 0.34 0.04 ± 0.48	0.71 ± 0.10 0.94 ± 0.10	0.27 ± 0.45 -0.03 ± 0.39	8.5 ± 5.4 4.1 ± 2.4	4.9 ± 25.7 7.3 ± 8.3
J1751+09	KD/UD+U3	0.34 ± 0.14	0.92 ± 0.28	\dots	\dots	\dots	\dots
J1927+73	KD+K3/UD+U3 K2/U2 K1/U1	0.11 ± 0.06 -0.59 ± 0.14 -0.79 ± 0.18	-0.32 ± 0.18 0.79 ± 0.34 1.24 ± 0.24	\dots 0.87 ± 0.08 0.99 ± 0.05	\dots 0.02 ± 0.31 0.17 ± 0.17	\dots 4.0 ± 4.5 -1.8 ± 1.6	\dots -12.0 ± 16.0 3.3 ± 5.6
J2005+77	KD+K2/UD+U3+U2 K1/U1	0.17 ± 0.11 -1.21 ± 0.24	0.71 ± 0.21 0.31 ± 0.87	1.20 ± 0.15 \dots	-0.18 ± 0.57 \dots	0.2 ± 1.8 \dots	5.4 ± 6.1 \dots

Note. — Spectral properties taken between 15 and 22 GHz. Mean values across epoch and slopes versus time are given for the spectral index, α ($S \propto \nu^{+\alpha}$), the fractional ratio, $m_{ratio} = m_{15}/m_{22}$, and the polarization position angle difference, $\Delta \chi = \chi_{15} - \chi_{22}$.

TABLE 8
EMPIRICAL UNCERTAINTY ESTIMATES.

Object	Jet Feature	$\sigma I_{15}/\langle I_{15} \rangle$	$\sigma I_{22}/\langle I_{22} \rangle$	σm_{15} (%)	σm_{22} (%)	$\sigma \chi_{15}$ (deg.)	$\sigma \chi_{22}$ (deg.)
3C 120	KD+K3+K2/UD+U2 K1A+K1B/U1A+U1B	0.07 (+0.05, -0.08) 0.09 (+0.04, -0.05)	0.08 (+0.06, -0.09) 0.10 (+0.05, -0.06)	0.3 (+0.2, -0.2)	0.6 (+0.4, -0.6)	5.0 (+1.7, -2.5)	10.6 (+3.6, -5.3)
J0530+13	KD+K2/UD+U2	0.03 (+0.02, -0.03)	0.03 (+0.02, -0.03)	0.5 (+0.3, -0.3)	0.6 (+0.4, -0.4)	5.5 (+4.1, -6.7)	3.3 (+2.5, -4.1)
J0738+17	KALL/UALL	0.02 (+0.01, -0.01)	0.09 (+0.05, -0.05)
OJ287	KD+K4/UD+U4 K3/U3	0.06 (+0.04, -0.05) 0.12 (+0.09, -0.15)	0.10 (+0.07, -0.08) 0.08 (+0.06, -0.09)	0.4 (+0.3, -0.3) 0.6 (+0.5, -0.9)	0.3 (+0.2, -0.3) 0.5 (+0.4, -0.8)	5.2 (+4.0, -7.0) 2.1 (+1.5, -2.3)	5.3 (+4.1, -7.1) 3.1 (+2.2, -3.4)
J1224+21	KD+K4+K3/UD+U3	0.05 (+0.04, -0.06)	0.03 (+0.02, -0.04)	0.6 (+0.3, -0.3)	0.2 (+0.1, -0.1)	1.7 (+1.3, -2.2)	1.7 (+1.3, -2.1)
3C 273	KD+K10/UD+U10 K9+K8+K7/U9+U8+U7 K4+K5/U4+U5	0.11 (+0.07, -0.08) 0.04 (+0.01, -0.02) 0.03 (+0.02, -0.02)	0.12 (+0.08, -0.08) 0.17 (+0.05, -0.08) 0.07 (+0.04, -0.04)	...	0.5 (+0.0, -0.2) 0.4 (+0.2, -0.3) 0.5 (+0.3, -0.4)	3.1 (+0.9, -1.3) 3.2 (+1.9, -2.0)	1.9 (+0.6, -0.8) 10.4 (+6.0, -6.6)
3C 279	KD+K4/UD+U4 K1+K2/U1+U2	0.03 (+0.02, -0.03) 0.05 (+0.01, -0.02)	0.03 (+0.02, -0.04) 0.02 (+0.00, -0.01)	0.5 (+0.3, -0.3) 1.1 (+0.4, -0.5)	0.8 (+0.4, -0.5) 1.1 (+0.4, -0.5)	8.9 (+4.8, -5.2) 1.5 (+0.0, -0.5)	4.4 (+2.4, -2.6) 4.0 (+0.0, -1.3)
J1310+32	KALL/UALL	0.03 (+0.00, -0.01)	0.12 (+0.00, -0.04)	0.4 (+0.2, -0.2)	0.3 (+0.1, -0.2)	3.4 (+2.5, -4.3)	5.6 (+4.2, -7.1)
J1512-09	KD+K2/UD+U2 K1/U1	0.05 (+0.03, -0.04) 0.06 (+0.01, -0.02)	0.05 (+0.03, -0.04) 0.10 (+0.01, -0.04)	0.5 (+0.1, -0.2) 1.1 (+0.0, -0.3)	0.8 (+0.1, -0.3) 1.0 (+0.0, -0.3)	10.0 (+7.6, -12.5) 3.0 (+1.9, -2.2)	9.7 (+7.4, -12.1) 3.7 (+2.4, -2.8)
J1751+09	KD/UD+U3	0.10 (+0.07, -0.08)	0.09 (+0.06, -0.07)
J1927+73	KD+K3/UD+U3 K2/U2 K1/U1	0.04 (+0.00, -0.01) 0.04 (+0.02, -0.02) 0.02 (+0.02, -0.02)	0.02 (+0.00, -0.01) 0.07 (+0.03, -0.04) 0.05 (+0.03, -0.04)	...	0.5 (+0.2, -0.8) 1.5 (+0.2, -0.8) 1.8 (+0.6, -0.9)	3.9 (+0.0, -1.3) 1.9 (+0.0, -0.6)	6.9 (+0.0, -2.3) 3.5 (+0.0, -1.2)
J2005+77	KD+K2/UD+U3+U2 K1/U1	0.02 (+0.02, -0.03) 0.06 (+0.00, -0.02)	0.01 (+0.01, -0.02) 0.19 (+0.00, -0.07)	0.6 (+0.3, -0.3) ...	0.9 (+0.5, -0.5) ...	3.3 (+2.1, -2.4) ...	2.8 (+1.8, -2.1) ...

Note. — These represent empirical estimates of the uncertainty in single-epoch measurements of the flux (I), the fractional polarization (m), and polarization position angle (χ) of jet features in our survey. Estimates are made for both 15 and 22 GHz.